

Journal of Geophysical Research: Oceans

RESEARCH ARTICLE

10.1002/2016JC012265

Key Points:

- A subgrid closure for mesoscale ocean LES is introduced
- The new closure is flow and scale-aware and specifies the Gent and McWilliams transport coefficient
- The new closure compares favorably to extant closures in truncating the cascades of energy and potential enstrophy

Correspondence to:S. Bachman,
sb965@cam.ac.uk**Citation:**

Bachman, S. D., B. Fox-Kemper, and B. Pearson (2017), A scale-aware subgrid model for quasi-geostrophic turbulence, *J. Geophys. Res. Oceans*, 122, 1529–1554, doi:10.1002/2016JC012265.

Received 22 AUG 2016

Accepted 31 JAN 2017

Accepted article online 7 FEB 2017

Published online 25 FEB 2017

A scale-aware subgrid model for quasi-geostrophic turbulence

Scott D. Bachman¹ , Baylor Fox-Kemper² , and Brodie Pearson²

¹Department of Applied Mathematics and Theoretical Physics, University of Cambridge, Cambridge, UK, ²Department of Earth, Environmental, and Planetary Sciences, Brown University, Providence, Rhode Island, USA

Abstract This paper introduces two methods for dynamically prescribing eddy-induced diffusivity, advection, and viscosity appropriate for primitive equation models with resolutions permitting the forward potential enstrophy cascade of quasi-geostrophic dynamics, such as operational ocean models and high-resolution climate models with $\mathcal{O}(25)$ km horizontal resolution and finer. Where quasi-geostrophic dynamics fail (e.g., the equator, boundary layers, and deep convection), the method reverts to scalings based on a matched two-dimensional enstrophy cascade. A principle advantage is that these subgrid models are scale-aware, meaning that the model is suitable over a range of grid resolutions: from mesoscale grids that just permit baroclinic instabilities to grids below the submesoscale where ageostrophic effects dominate. Two approaches are presented here using Large Eddy Simulation (LES) techniques adapted for three-dimensional rotating, stratified turbulence. The simpler approach has one nondimensional parameter, Λ , which has an optimal value near 1. The second approach dynamically optimizes Λ during simulation using a test filter. The new methods are tested in an idealized scenario by varying the grid resolution, and their use improves the spectra of potential enstrophy and energy in comparison to extant schemes. The new methods keep the gridscale Reynolds and Péclet numbers near 1 throughout the domain, which confers robust numerical stability and minimal spurious diapycnal mixing. Although there are no explicit parameters in the dynamic approach, there is strong sensitivity to the choice of test filter. Designing test filters for heterogeneous ocean turbulence adds cost and uncertainty, and we find the dynamic method does not noticeably improve over setting $\Lambda = 1$.

1. Introduction

Turbulence in the ocean is heterogeneous, anisotropic, and scale-dependent; from region to region, direction to direction, and season to season, the character of oceanic turbulence changes. Oceanic turbulence on the largest, slowest scales is strongly affected by the rotation and curvature of the Earth, while on the smallest scales is akin to turbulence studied in wind tunnels and laboratories. Large-scale turbulence is also flattened into nearly two-dimensional flow by the thin aspect ratio of the ocean (10,000 km wide and 4 km deep) and by the oceanic density stratification that makes lifting deeper, denser water to the surface energetically costly.

The complexity and variety of oceanic flows has motivated rapid improvements in the model resolution of ocean general circulation models. At present, many modeling centers worldwide are poised to enter a new regime of modeling, where mesoscale eddies occur naturally across nearly the whole globe. These prototype eddy-rich models show dramatic promise of realism [Berloff *et al.*, 2007; Bryan *et al.*, 2010; Penduff *et al.*, 2010; McClean *et al.*, 2011; Kirtman *et al.*, 2012; Delworth *et al.*, 2012; Jochum *et al.*, 2013; Frenger *et al.*, 2013; Treguier *et al.*, 2014; Mizielski *et al.*, 2014]. However, their enormous computational cost means that they are run only a handful of times, limiting the parameter exploration that has traditionally been used to optimize coarser resolution models [e.g., Jochum *et al.*, 2008]. Despite their higher resolution, some aspects of the climate in these prototype models may be farther from observations when compared to the heavily tuned, but coarse-resolution, models [e.g., Bryan *et al.*, 2014].

Both eddy-permitting and eddy-resolving models offer potential for realism and novel dynamics but also require greater care. Eddy parameterizations such as the popular [Gent and McWilliams, 1990, hereafter GM] and Redi [1982] adiabatic eddy-induced advection and diffusion schemes are routinely employed in coarsely

resolved models where eddies are absent. Extending the key ideas of these schemes into the eddy-rich regime, where the model resolves the largest eddies, is usually avoided. Instead, physical parameterizations are often turned off to retain only the minimum numerical closure needed to keep models stable [McClean *et al.*, 2011; Delworth *et al.*, 2012; Bryan *et al.*, 2014] and avoid double-counting of eddies in both resolved and parameterized form. Typically, preserving physical parameterizations while changing only resolution tends to result in anemic eddies that fail to compete with the parameterizations for available potential energy or are damped by parameterizations directly [e.g., Hallberg, 2013]. On the other hand, turning off the parameterizations at relatively coarse, but still eddy-permitting, resolution tends toward underestimating important effects of the smaller eddies that are not resolved in tracer transport, variance reduction, and restratification. Furthermore, many studies attempting to optimize blends of subgrid models have shown that the choice of subgrid models and their parameter tuning remains important even at high resolution [e.g., Chassignet and Garraffo, 2001; Fox-Kemper and Menemenlis, 2008; Hecht *et al.*, 2008].

An important consideration in modeling is whether there is a scale separation between the resolved features and the dominant eddy scale. Based on the scale separation and related closure choices, a model can be considered to be a Reynolds-Averaged (RANS) model or a Large Eddy Simulation (LES). The distinction between RANS and LES is commonly made in engineering turbulence literature [Sagaut, 2005], but it is appropriate for mesoscale ocean models as well [Fox-Kemper and Menemenlis, 2008]. The third category of direct numerical simulation, where the Navier-Stokes equations are solved directly with realistic values of all parameters, is not relevant for large-scale oceanography. A subclass of LES known as very large eddy simulations also have been considered in the context of ocean modeling [e.g., Ilicak *et al.*, 2008], for which the techniques discussed here can also be applied.

If a scale separation exists between the scale of the eddies and the scale of the grid, or the eddies are handled statistically [e.g., Farrell and Ioannou, 1993; Dukowicz and Smith, 1997], then repeated averaging at the gridscale does not change the result (averaging is idempotent) and a traditional Reynolds-averaging procedure applies. Thus, for any flow variable ϕ , $\bar{\phi} = \overline{\phi}$ and a deviation can be denoted by $\phi' = \phi - \bar{\phi}$, and $\phi\varphi = \bar{\phi}\bar{\varphi} + \phi'\varphi'$. A large-scale separation also implies that changing the resolution of the model should not change the degree to which the subgrid-scale processes are resolved (i.e., they are much smaller still), so the effects of the small, unresolved scales on the large, resolved scales should not depend sensitively on model resolution. The resolved model variables provide $\bar{\phi}\bar{\varphi}$ but not $\phi'\varphi'$, so a resolution-independent estimate based on resolved properties—called a *parameterization* in Reynolds-averaged ocean models—is used to close the equations. Usually, only nonlinear terms require parameterization, as these terms connect disparate scales and rectify upon averaging. By contrast, LES do not assume a scale separation at the gridscale, thus the gridscale is considered as a filter, called the grid filter, and $\bar{\phi} \neq \overline{\phi}$. Even in LES, the equations of motion for the resolved variables underestimate or misestimate covariances when the resolved flow is used, so corrections arise of the form $\overline{\phi\varphi} - \bar{\phi}\bar{\varphi}$ [Leonard, 1974]. Again, $\bar{\phi}\bar{\varphi}$ is directly calculated from resolved variables, but the total $(\overline{\phi\varphi})$ is not. Providing an approximation to the correction, $\overline{\phi\varphi} - \bar{\phi}\bar{\varphi}$, in LES is called a *subgrid model*, and it closes the set of equations just as a parameterization does. Ideally, the total $(\overline{\phi\varphi})$ ought not depend on resolution, but the corrections $(\overline{\phi\varphi} - \bar{\phi}\bar{\varphi})$ are expected to depend on resolution as varying the gridscale without scale separation affects what fraction of the total is resolved. Here we will use parameterization and subgrid model to refer to Reynolds-average and LES closures, respectively.

Eddy-rich models generally resolve the largest baroclinic and barotropic eddies, but not eddies of limited vertical scale or farther down a cascade, such as frontal and submesoscale eddies [Boccaletti *et al.*, 2007; Fox-Kemper *et al.*, 2011; Bachman and Taylor, 2014]. Baroclinic and barotropic instabilities produce the largest eddies near the front width or first baroclinic Rossby deformation radius: about 10–200 km depending on latitude and stratification [Chelton *et al.*, 1998; Hallberg, 2013]. As in Fox-Kemper and Menemenlis [2008], mesoscale-eddy-rich models with subgrid models to handle partially resolved eddies will be called Mesoscale Ocean Large Eddy Simulations (MOLES). There are a number of approaches for idealized and realistic MOLES in the literature [e.g., Willebrand *et al.*, 2001; Fox-Kemper and Menemenlis, 2008; Chen *et al.*, 2011; Nadiga and Bouchet, 2011; Nguyen *et al.*, 2011; San *et al.*, 2013], and a variety of applications for eddy-rich ocean modeling where improved MOLES subgrid models would be beneficial [e.g., Penduff *et al.*, 2010; Scott *et al.*, 2010; McClean *et al.*, 2011; Delworth *et al.*, 2012; Ringler *et al.*, 2013; Treguier *et al.*, 2014; Blaker *et al.*, 2015; Brassington *et al.*, 2015].

Subgrid models automatically adjust their effects as resolution, grid orientation, and the resolved flow change based on physical principles, the detection of key measures from the resolved flow (flow-awareness), and the ability of the model grid to represent such effects (scale-awareness). Scale-awareness can be built into subgrid models, but it is much more convincing when it arises naturally as a product of the theory underpinning the subgrid model. For example, the basic Smagorinsky [1963] model is flow-aware and scale-aware through a specified rate of dissipation of resolved energy. Fox-Kemper *et al.* [2011] generalize a submesoscale parameterization designed for mesoscale-resolving models to a form suitable for coarser models and arrive at scale-awareness as a by-product. Chen *et al.* [2011] convert a nonscale-aware parameterization with dimensional parameters into a scale-aware subgrid model with only dimensionless parameters. Hallberg [2013] uses scale-awareness to determine when and where to use parameterizations.

The dynamics that support the development of a MOLES subgrid model are not the same as those for traditional LES, as the scale and aspect ratio of flows in MOLES are dominated by stratification and rotation effects, and the curvature of the earth may be important. Such a flow is dominantly geostrophic on a rotating plane, and ageostrophic only at higher order to include the effects of relative vorticity, vortex stretching, planetary curvature, etc. In this regime, the appropriate reduced dynamics are quasi-geostrophic (QG) [Charney, 1971; Pedlosky, 1987; Vallis, 2006]. Where QG is inappropriate, two-dimensional (2-D) fluid dynamics is usually the next most natural flow regime after QG, rather than three-dimensional (3-D) dynamics. For example, near the equator vertical planetary rotation is small, but global model grids are wide and shallow and stratification is strong, leading to quasi-2-D resolved dynamics along density surfaces. In surface or bottom boundary layers, QG fails as stratification is weak, but the wide and shallow gridscale continues to select (rotating) 2-D along-surface dynamics. The approach here combines 2-D and QG phenomenology into subgrid model closures appropriate for use in 3-D MOLES.

This paper generalizes (section 2) and evaluates (section 3) flow-aware, scale-aware subgrid models based on the Leith [1996] subgrid model for viscosity in 2-D turbulence in a potential enstrophy turbulent cascade. The Leith scheme performs well as a subgrid model for 2-D LES [Pietarila Graham and Ringler, 2013] and can be adequately adapted for the 3-D MOLES setting [Fox-Kemper and Menemenlis, 2008]. The scale-awareness of the Leith scheme arises naturally from 2-D turbulence theory. Exploiting the similarities between 2-D and QG dynamics [Charney, 1971] allows extension of the Leith scheme to resemble QG dynamics. Unlike the 2-D theory, the QG theory (section 2.4) naturally incorporates adiabatic advection and diffusion from the Gent and McWilliams [1990] and Redi [1982] parameterizations into a scale-aware, flow-aware form suitable for use as a MOLES subgrid closure, as suggested by Roberts and Marshall [1998]. The QG subgrid model has one dimensionless parameter. Inspired by techniques drawn from the LES literature [e.g., Germano *et al.*, 1991; Lilly, 1992], a dynamical method to eliminate this parameter by relating the smallest and near-smallest resolved scales is also presented (section 2.8). Idealized simulations with a potential enstrophy cascade of varying depth (similar to Bachman and Fox-Kemper [2013] and Bachman *et al.* [2015]) are used to test the new methods versus extant MOLES subgrid models (section 3). Implications of the new method are discussed in section 4.

2. Background and Theory

A few key concepts are needed from 2-D, QG, and Boussinesq ocean dynamics to frame the presentation of the subgrid models. Sections 2.1 and 2.2 will present the dimensionless equations written with dimensionless variables and parameters to establish the relative importance of different terms in the equations. All other sections will use dimensional variables.

2.1. Dimensionless Parameters Using the Gridscale

For the purposes of developing subgrid models convenient dimensionless parameters are formed using the following scales. Here the horizontal velocity will be denoted \mathbf{v}_h , the vertical velocity w , and perturbation pressure p . A linear equation of state will be assumed which splits the buoyancy b , potential temperature θ , and salinity S into mean (denoted by an overbar) and perturbation components, so that $\bar{b}(z) + b(x, y, z, t) = g(\alpha[\bar{\theta} + \theta] - \beta[\bar{S} + S])$. The linearity of the equation of state will be assumed to be local, so that α, β may vary but their gradients will be neglected in favor of the larger S, θ variations here, e.g., (8). Here either salinity and potential temperature or absolute salinity and conservative temperature are used [Wright *et al.*, 2011].

The length scales are those of the discretized grid, assigned as $\Delta s = \sqrt{\Delta x \Delta y}$ for the horizontal grid spacing and Δz for the vertical grid spacing, and f_0 is the local Coriolis parameter. Following Fox-Kemper and Mennelis [2008], an asterisk denotes resolved model fields, as opposed to the abstract field variables

$$\mathbf{v}_h \sim V_* \quad w \sim \pi_0 V_* / N_*^2 \Delta z \Delta s \quad p \sim \pi_0 = \max(V_* f_0 \Delta s, V_*^2), \quad (1a)$$

$$b \sim \pi_0 / \Delta z \quad \theta \sim \pi_0 / \Delta z g \alpha \quad S \sim \pi_0 / \Delta z g \beta, \quad (1b)$$

$$\partial_z \bar{b} \sim N_*^2 \quad \partial_z \bar{\theta} \sim N_*^2 / g \alpha \partial_z \quad \bar{S} \sim N_*^2 / g \beta. \quad (1c)$$

Along with the horizontal viscosity, v_* , and diffusivity, κ_* , the relevant nondimensional parameters are the grid Rossby number ($\text{Ro}_* = V_* / f_0 \Delta s$), baroclinic Froude number (see below), planetary number ($\text{Pl}_* = \Delta y \frac{\partial f}{\partial y} / f_0$), aspect ratio ($\delta = \Delta z / \Delta s$), Reynolds number ($\text{Re}_* = V_* \Delta s / v_*$), and Péclet number ($\text{Pe}_* = V_* \Delta s / \kappa_*$). The asterisks on viscosity and diffusivity within the Reynolds and Péclet number imply the use of “eddy” viscosity and diffusivity in models, or more generally the ratio of the resolved flux divergence to the subgrid model flux divergence. To compare the gridscale Δs to the first baroclinic deformation radius L_d , the WKBJ estimate of the first deformation radius from Chelton *et al.* [1998] is useful,

$$L_d = \frac{1}{|f| \pi} \int_{-H}^0 N(z) dz. \quad (2)$$

If the Froude number is defined similarly [LeBlond and Mysak, 1981], then

$$\text{Fr}_* = \frac{V_* \pi}{\int_{-H}^0 N_*(z) dz}. \quad (3)$$

The gridscale Burger number (Bu_*) relates the deformation radius to gridscale: $L_d / \Delta s = \text{Ro}_* / \text{Fr}_* = \sqrt{Bu_*}$, and a large Burger number implies a well-resolved mesoscale.

2.2. Turbulence Differs by Scale

The scalings above are used to span from QG scaling to stratified turbulence scaling following McWilliams [1985] but retaining dissipation terms. Only the leading order term involving Pl_* is retained, given its small size on eddy-rich grids (section 2.6). The result is

$$\text{Ro}_* [\partial_t \mathbf{v}_h + \mathbf{v}_h \cdot \nabla \mathbf{v}_h + \epsilon w \partial_z \mathbf{v}_h] + \underbrace{\left(1 + \frac{y \text{Pl}_*}{\Delta y}\right) \hat{\mathbf{z}} \times \mathbf{v}_h + M_{R_*} \nabla_h \pi}_{\text{geostrophic}} = \frac{\text{Ro}_*}{\text{Re}_*} \nabla \cdot \mathbf{D}_{\mathbf{v}_h}, \quad (4)$$

$$\text{Fr}_*^2 \frac{\Delta z^2}{\Delta s^2} [\partial_t w + \mathbf{v}_h \cdot \nabla w + \epsilon w \partial_z \mathbf{v}_h] + \underbrace{\partial_z \pi - \hat{\mathbf{z}} b}_{\text{hydrostatic}} = \frac{\text{Fr}_*^2 \Delta z^2}{\text{Re}_* \Delta s^2} \nabla \cdot \mathbf{D}_w, \quad (5)$$

$$\partial_t S + \mathbf{v}_h \cdot \nabla S + \epsilon w \partial_z S + w \partial_z \bar{S} = \frac{1}{\text{Pe}_*} \nabla \cdot \mathbf{D}_S, \quad (6)$$

$$\partial_t \theta + \mathbf{v}_h \cdot \nabla \theta + \epsilon w \partial_z \theta + w \partial_z \bar{\theta} = \frac{1}{\text{Pe}_*} \nabla \cdot \mathbf{D}_\theta, \quad (7)$$

$$\partial_t b + \mathbf{v}_h \cdot \nabla b + \epsilon w \partial_z b + w \partial_z \bar{b} = \frac{1}{\text{Pe}_*} \nabla \cdot (\alpha \mathbf{D}_\theta - \beta \mathbf{D}_S), \quad (8)$$

$$\nabla \cdot \mathbf{v}_h + \epsilon \partial_z w = 0, \quad (9)$$

$$M_{R_*} \equiv \max(1, \text{Ro}_*), \quad \epsilon \equiv \frac{\text{Fr}_*^2}{\text{Ro}_*} M_{R_*} = \begin{cases} \text{Fr}_*^2 & \text{Ro}_* \geq 1 \\ \text{Ro}_* \text{Bu}_*^{-1} & \text{Ro}_* < 1 \end{cases}. \quad (10)$$

Dissipation terms are expressed as divergences of dissipative fluxes, ensuring global conservation even with variable coefficients. Note that $\mathbf{D}_{\mathbf{v}_h}$, \mathbf{D}_w represent projections of an overall (symmetric) stress tensor \mathbf{D}_v into horizontal and vertical directions.

It is useful to introduce a (vertical component of a) stream function ψ and potential χ , as well as a vertical component of vorticity q_2 . These variables obey a 2-D vorticity equation (11) and other constraints

$$\partial_t q_2 + J(\psi, q_2) - D_{q_2} = \epsilon \partial_z w + \mathcal{O}(\text{Ro}_*, \text{Pl}_*, \epsilon), \quad (11)$$

$$\nabla_h^2 \psi = M_{R_*} \nabla_h^2 \pi + 2\text{Ro}_* J(\partial_x \psi, \partial_y \psi) + \mathcal{O}(\text{Pl}_*, \text{Ro}_*, \epsilon), \quad (12)$$

$$\partial_z \pi = b + \mathcal{O}(\text{Fr}_*^2 \Delta z^2 / \Delta s^2), \quad (13)$$

$$\mathbf{v}_h = \hat{\mathbf{z}} \times \nabla \psi + \epsilon \nabla \chi, \quad q_2 = 1 + \text{Ro}_* \nabla_h^2 \psi + \frac{\text{Pl}_* y}{\Delta y}, \quad \partial_z w = -\nabla_h^2 \chi, \quad (14)$$

$$D_{q_2} = \frac{\text{Ro}_*}{\text{Re}_*} \nabla \cdot (\hat{\mathbf{z}} \times \nabla \mathbf{D}_{\mathbf{v}_h}). \quad (15)$$

Recalling that numerical stability requires Re_* be $\mathcal{O}(1)$, the dissipation term D_{q_2} is $\mathcal{O}(\text{Ro}_*)$ at the gridscale in (11). The vortex stretching term $\partial_z w$ scales as $\mathcal{O}(\epsilon)$, while the dynamical components of q_2 scale as Ro_*, Pl_* .

By using (11)–(13) with (8), the vertical velocity can be eliminated resulting in the quasi-geostrophic potential vorticity (QGPV; $q_q = q_2 + \partial [f^2 / N^2 (\partial \psi / \partial z)] / \partial z$) equation (16),

$$\partial_t q_q + J(\psi, q_q) - D_{q_q} = \mathcal{O}(\epsilon \text{Ro}_*/M_{R_*}, \epsilon \text{Pl}_*/M_{R_*}), \quad (16)$$

$$q_q = 1 + \text{Ro}_* \left(\nabla_h^2 \psi + \text{Bu}_*^{-1} \partial_z \frac{\partial_z \psi}{\partial_z b} \right) + \frac{\text{Pl}_* y}{\Delta y}, \quad (17)$$

$$D_{q_q} = D_{q_2} + \frac{\epsilon}{\text{Pe}_*} \partial_z \frac{\nabla \cdot \alpha \mathbf{D}_\theta}{\partial_z b} - \frac{\epsilon}{\text{Pe}_*} \partial_z \frac{\nabla \cdot \beta \mathbf{D}_S}{\partial_z b}. \quad (18)$$

The QG dissipation term D_{q_q} cannot be written as the divergence of a flux generally, and D_{q_2} is written similarly in (15).

2.2.1. Kolmogorov and Smagorinsky 3-D Turbulence

Three-dimensional, nonrotating, unstratified turbulence occurs on small, fast scales in the limit of $\text{Re}_* \gg 1, \text{Fr}_* \gg 1, \epsilon \gg 1, \Delta z \sim \Delta s$, in which case equations (4–9) reveal that geostrophy and hydrostasy are subdominant. Despite the fact that this limit is never realized in large-scale ocean modeling ($\Delta s \gg \Delta z$), it is the foundation of the development of the theory of inertial ranges and flow-aware, scale-aware LES subgrid models [Kolmogorov, 1941; Smagorinsky, 1963, 1993]. The theory stems from the budget of total kinetic energy, which is the domain-average of the dot product of the momentum equations with the velocities.

$$\bar{E} = \frac{1}{V} \int_V \frac{1}{2} \mathbf{v} \cdot \mathbf{v} dV = \frac{1}{2} \langle \mathbf{v} \cdot \mathbf{v} \rangle = \int_0^\infty E(k) dk, \quad (19)$$

$$\frac{d\bar{E}}{dt} = \varepsilon + \langle \mathbf{v} \cdot (\nabla \cdot \mathbf{D}_v) \rangle. \quad (20)$$

Energy is produced (possibly by both shear and buoyancy production) or otherwise injected at a rate ε on a scale (production wave number: k_p) far larger than the scale at which it is dissipated (dissipation wave number: k_d , $k_d \gg k_p$). In between these scales ($k_p < k < k_d$) and in statistically steady state, Kolmogorov [1941] argues that the energy spectrum $E(k)$ can only depend on the local scale k and ε , so by dimensional analysis $E(k) \propto \varepsilon^{2/3} k^{-5/3}$ and $k_d = \varepsilon^{1/4} v^{-3/4}$. Smagorinsky [1963, 1993] argues that resolved dissipation must balance the energy production, which is equal to the energy transfer through every scale in the cascade. Thus, if an isotropic viscosity v_* (larger than the true viscosity) is applied to the resolved flow and the maximum resolved wave number $k_* = \pi / \Delta s$ is taken proportional to k_d with a constant Υ ,

$$k_* = \Upsilon \varepsilon^{1/4} v_*^{-3/4}, \quad (21)$$

$$\varepsilon = -\langle \mathbf{v}_* \cdot (\nabla \cdot \mathbf{D}_{v_*}) \rangle = \langle \frac{v_*}{4} (\partial_j u_{*i} + \partial_i u_{*j}) (\partial_j u_{*i} + \partial_i u_{*j}) \rangle. \quad (22)$$

The form of the dissipation on the right-hand side of (22) involves manipulation and integration by parts (using suitable boundary conditions) to arrive at a positive-definite form. By replacing the domain average in (22) with a local value, a viscosity can be found that supplies the needed energy dissipation,

$$v_* = \left(\frac{\Upsilon}{k_*}\right)^2 |D_*| = \left(\frac{\Upsilon \Delta s}{\pi}\right)^2 |D_*|, \quad (23)$$

$$|D_*| = \sqrt{\frac{1}{4} (\partial_j u_{*i} + \partial_i u_{*j}) (\partial_j u_{*i} + \partial_i u_{*j})}. \quad (24)$$

This conversion from domain average to local value is a prime reason to doubt the Smagorinsky theory [Lesieur *et al.*, 2005], and another is the fact that energy fluxes within an inertial range tend to be spectrally long-range rather than local [e.g., Rubio *et al.*, 2014]. These deficiencies are common to all of the cascade subgrid models presented. Other objections to the Smagorinsky approach are more relevant in engineering-scale flows in bounded domains [Piomelli and Zang, 1991; Meneveau and Katz, 2000; Geurts and Holm, 2006; Mohseni *et al.*, 2003]. The dimensionless constant Υ is taken to be 1. Sometimes the dependence on this single, constant parameter is also considered to be a deficiency (see section 2.8). In the hydrostatic limit ($Fr_*^2 \Delta z^2 \ll \Delta s$), the strain rate is approximated from horizontal velocities only,

$$|D_*| = \sqrt{[\partial_x u_* - \partial_y v_*]^2 + [\partial_y u_* + \partial_x v_*]^2 + \mathcal{O}(\epsilon V_* / \Delta s)}. \quad (25)$$

Note that the relative signs of the components in the horizontal strain rate are unlike those in the vorticity and divergence, which can lead to coding errors.

2.3. Kraichnan and Leith 2-D Turbulence

When $\epsilon \ll Ro_*, Pl_*$ or $Bu_* \gg 1$, then the stretching terms in (11) and (16) and the temperature and salinity diffusion in (18) are negligible. In this limit, the vertical vorticity equation (11) is a closed system that predicts vorticity and the leading order horizontal velocity from ψ if D_{q_2} can be appropriately supplied and higher-order terms on the right side of (11) are neglected.

Without D_{q_2} , the kinetic energy (\bar{E}) is conserved in 2-D turbulence

$$\bar{E} = \frac{1}{2} \langle \mathbf{v}_h \cdot \mathbf{v}_h \rangle = \frac{1}{2} \langle |\nabla_h \psi|^2 \rangle = -\langle \psi q_2 \rangle = \int_0^\infty E(k) dk, \quad (26)$$

$$\frac{d\bar{E}}{dt} = \epsilon + \langle \psi D_{q_2} \rangle. \quad (27)$$

In addition to \bar{E} , Kraichnan [1967] notes that domain-averaged enstrophy \bar{Z} is also conserved in 2-D turbulence without D_{q_2} , as demonstrated by multiplying the vorticity equation by vorticity and domain averaging

$$\bar{Z} = \frac{1}{2} \langle (\hat{\mathbf{f}} \hat{\mathbf{z}} + \nabla \times \mathbf{v}_h) \cdot (\hat{\mathbf{f}} \hat{\mathbf{z}} + \nabla \times \mathbf{v}_h) \rangle = \frac{1}{2} \langle q_2^2 \rangle = \int_0^\infty Z(k) dk, \quad (28)$$

$$\frac{d\bar{Z}}{dt} = \eta_2 + \langle q_2 D_{q_2} \rangle. \quad (29)$$

Proceeding along the same lines as Kolmogorov [1941], Kraichnan [1967] finds two different inertial ranges are consistent with the simultaneous conservation of \bar{E} and \bar{Z} , but now it is the enstrophy which is produced at a rate η_2 on a scale far larger than the scale at which it is dissipated. For scales larger than the production or injection scale ($k < k_p$), an inverse cascade of energy is expected where $E(k) \propto \epsilon^{2/3} k^{-5/3}$, $Z(k) \propto \epsilon^{2/3} k^{1/3}$ and enstrophy does not cascade. For scales smaller than the injection/production scale ($k_p < k < k_d$) a forward cascade of enstrophy may exist where $E(k) \propto \eta_2^{2/3} k^{-3}$, $Z(k) \propto \eta_2^{2/3} k^{-1}$, $k_d = \eta_2^{1/6} \nu^{-1/2}$, and energy does not cascade.

Leith [1996] follows Smagorinsky [1963, 1993] to find a viscosity to halt the enstrophy cascade

$$k_* = \Lambda \eta_2^{1/6} \nu_*^{-1/2}, \quad (30)$$

$$\eta_2 = -\langle q_2 \cdot D_{q_2} \rangle \approx \langle v_* \nabla q_{2*} \cdot \nabla q_{2*} \rangle, \quad (31)$$

$$\nu_* = \left(\frac{\Lambda}{k_*}\right)^3 |\nabla_h q_{2*}| = \left(\frac{\Lambda \Delta s}{\pi}\right)^3 |\nabla_h (\hat{\mathbf{f}} \hat{\mathbf{z}} + \nabla \times \mathbf{v}_{h*})|, \quad (32)$$

$$\nabla \cdot \mathbf{D}_{\mathbf{v}_h} = \nabla_h \cdot v_* \nabla_h \mathbf{v}_{h*} + \text{vertical viscosity}. \quad (33)$$

The approximation in (31) neglects a term resulting from spatial variation in v_* , along and consistent with the conversion from the average enstrophy production in (31) to a local value in (32). As in (23), the dimensionless constant Λ is taken to be 1.

A term of $\mathcal{O}(\text{Pl}_*)$ is added to form a positive definite right side of (31), and while it does not contribute in the domain average, it results in f appearing in (32) which does contribute to the viscosity. With equal asymptotic accuracy, an $\mathcal{O}(\text{Pl}_*)$ term might be dropped so that the viscosity was proportional to the relative, rather than absolute, vorticity gradient. Deciding between retention or neglect of this Coriolis term requires higher accuracy than the theory used to derive (32) (section 2.6), which was selected due to its similarity to the QG form below. Note that including this term in the approximation (31) leading to (32) affects the magnitude of the viscosity determined, but *does not imply violation* of the conservation of momentum, energy, or enstrophy when used in (33) and (4).

Vertical viscosity is also neglected in deriving (11). Although it can aid in halting the cascade of enstrophy, and D_{q_2} is the only mechanism of communication from one depth to another in this limit of (11), vertical viscosity ought not vary with horizontal resolution in MOLES and usually represents processes such as internal wave breaking that are not part of 2-D turbulence. The scaling in (31) assumes vertical viscosity is secondary in the cascade and provided from another theory.

Fox-Kemper and Menemenlis [2008] note that even though the divergence of the horizontal velocity is expected to be small in comparison to the vorticity, (32) leaves purely divergent motion undamped causing noisy vertical velocities. They propose the following modification to (32):

$$v_* = \left(\frac{\Lambda \Delta s}{\pi} \right)^3 \sqrt{|\nabla_h(f\hat{\mathbf{z}} + \nabla \times \mathbf{v}_h)|^2 + |\nabla_h(\nabla \cdot \mathbf{v}_h)|^2}. \quad (34)$$

2.4. Charney Quasi-Geostrophic (QG) Turbulence

Eddy-rich large or global-scale models have variations on a variety of scales. In models where the gridscale dimensionless parameters are asymptotically: $\text{Ro}_* \sim \text{Fr}_*^2 \sim \text{Pl}_* \ll 1$, $\Delta s \gg \Delta z$, $\text{Re}_* \sim 1$, $\text{Pe}_* \sim 1$, and $\text{Bu}_* \geq 1$, the gridscale dynamics are well-described by the dissipative QG potential vorticity equation (16), neglecting higher-order terms on the right-hand side. These parameter ranges are typical of models resolving the mesoscale and even many permitting the submesoscale. Unlike in 2-D turbulence (section 2.3), $\epsilon \sim \text{Ro}_*$, so the vortex stretching terms on the right side of (11) and in (16), as well as the temperature and salinity diffusion in (18), are at leading order. The guiding principle of this paper is that incorporating these terms into a subgrid model will improve the dynamics of MOLES. This approach follows closely the 2-D theory of Leith, so it will be called the QG Leith model.

The notation for QG in (16) is deliberately similar to that of 2-D dynamics (11), but stretching terms must be considered in the QG regime. *Charney* [1971] presented (16) and also noted the close similarity between the dynamics of this equation and those from (11) in terms of cascades and vortex interactions: an inverse energy cascade and a forward (potential) enstrophy cascade. Charney has six rules for QG cascade theory to apply, which can be taken here to govern when the QG Leith viscosity is appropriate. (1) The horizontal and rescaled vertical scale of the turbulence must be small in comparison to the deformation radius, i.e., $\text{Bu}_* \geq 1$. (2) $\text{Pl}_* \ll \text{Ro}_*$. (3) Stratification $\partial_z \bar{b}$ must vary more slowly than resolved motions. (4) The turbulence is approximately isotropic and homogeneous in horizontal planes. (5) The nonlinear interactions are local in wave number space. (6) The production rate and scale are sufficient for an inertial range to exist between k_p and the gridscale. If these rules hold, then (16) applies with a negligible right-hand side, and there is a forward cascade of potential enstrophy cascade which should exhibit $E(k) \propto \eta_q^{2/3} k^{-3}$, $Z(k) \propto \eta_q^{2/3} k^{-1}$. The conservation laws are

$$\bar{E} = -\frac{1}{2} \langle \psi q_q \rangle = \int_0^\infty E(k) dk, \quad \frac{d\bar{E}}{dt} = \epsilon + \langle \psi D_q \rangle, \quad (35)$$

$$\bar{Z} = \frac{1}{2} \langle q_q^2 \rangle = \int_0^\infty Z(k) dk, \quad \frac{d\bar{Z}}{dt} = \eta_q + \langle q_q D_{q_q} \rangle. \quad (36)$$

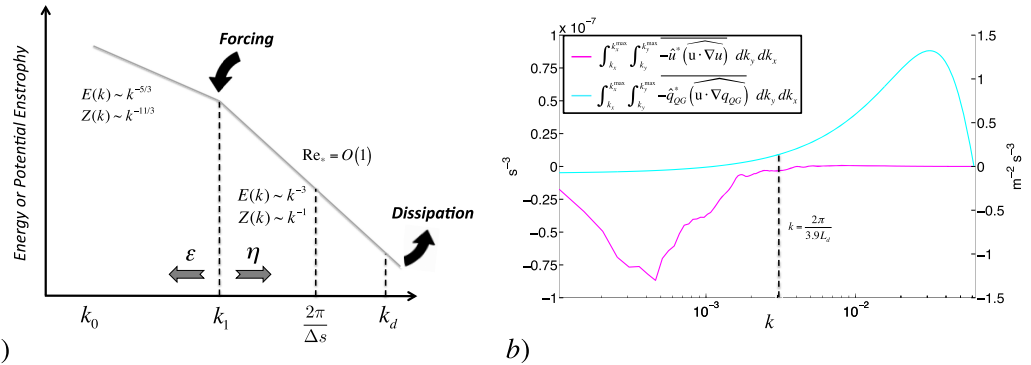


Figure 1. (a) Schematic of the cascades of energy and potential enstrophy in QG flow, with spectral slopes from Smith et al. [2002]. Energy and enstrophy are produced by instabilities near wave number k_1 , leading to an inverse cascade of energy toward the domain scale k_0 and a forward cascade of potential enstrophy toward the grid wave number $2\pi/\Delta s$. For a statistically steady state, a model must dissipate this energy and enstrophy appropriately. (b) Spectral fluxes of (purple) energy and (blue) potential enstrophy as a function of wavelength λ , taken from a simulation with $\Delta s = L_d/10.0$, $Bu_* = 100$. Negative values indicate a flux toward larger scales; positive values indicate fluxes toward smaller scales. The two cascades originate near the production scale, estimated here using the Eady [1949] fastest growing baroclinic instability wave number (black dashed vertical line).

The forward cascade of potential enstrophy in QG turbulence is naturally halted by the model grid, but this occurs independently of whether the correct amount of potential enstrophy is dissipated. Figure 1a shows a schematic of the cascades in QG flow, where the grid is envisioned to artificially truncate the forward cascade of potential enstrophy that would otherwise be dissipated at the Kolmogorov scale. Figure 1b exemplifies that the energy and enstrophy fluxes in the simulations in section 3 do indeed go upscale and downscale as in Figure 1a.

Nearly the same viscosity derivation applies in QG as in the 2-D case,

$$k_* = \Lambda \eta_q^{1/6} v_*^{-1/2}, \quad (37)$$

$$\eta_q = -\langle q_{q*} \cdot D_{q*} \rangle \approx \langle v_* \nabla_h q_{q*} \cdot \nabla_h q_{q*} \rangle, \quad (38)$$

$$v_* = \left(\frac{\Lambda}{k_*} \right)^3 |\nabla_h q_{q*}| = \left(\frac{\Lambda \Delta s}{\pi} \right)^3 |\nabla_h(f\hat{\mathbf{z}}) + \nabla_h(\nabla \times \mathbf{v}_{h*}) + \partial_z \frac{f}{N^2} \nabla_h b|. \quad (39)$$

When applying QG theory over planetary scales, it is important to distinguish between slowly varying components of buoyancy (b) and stratification (N^2) which are governed by planetary budgets and variations that occur on the mesoscale [Pedlosky, 1987, section 6.5]. QG theory predicts only the mesoscale variations, and takes N^2 and f as parameters. However, a global 3-D MOLES will predict all of these properties, and only through averaging or differentiation are they distinguished. In (39), the horizontal gradient in $\nabla_h q_q$ has been distributed out over the different terms in q_q to isolate b , which is allowed to vary in the horizontal in QG, from N^2 , which is not. In this form, no averaging is needed to distinguish between $N^2 = \partial_z \bar{b}$ and $N^2 \approx \partial_z \bar{b} + \partial_z b$.

As in 2-D, (39) does not constrain purely divergent motions such as internal waves, so a $\mathcal{O}(\epsilon)$ modification handles this problem,

$$v_* = \left(\frac{\Lambda \Delta s}{\pi} \right)^3 \sqrt{|\nabla_h(f\hat{\mathbf{z}}) + \nabla_h(\nabla \times \mathbf{v}_{h*}) + \partial_z \frac{f}{N^2} \nabla_h b|^2 + |\nabla[\nabla \cdot \mathbf{v}_h]|^2}. \quad (40)$$

This form can be used in all regions where QG dynamics are expected to apply. Similar caveats to (11) regarding the neglect of vertical viscosity in the derivation and inclusion of Coriolis terms in the vorticity magnitude apply to (40). A visualization of the viscosity field resulting from (40) is shown in Figure 2.

A major difference between QG and 2-D is hidden in (38), which can be found by comparing the dissipation operator in QG (18) to that in 2-D (15). In 2-D, relating dissipation of enstrophy (D_{q2}) to the positive-definite magnitude of the absolute vorticity squared requires only routine manipulation. Equation (31) requires us to relate

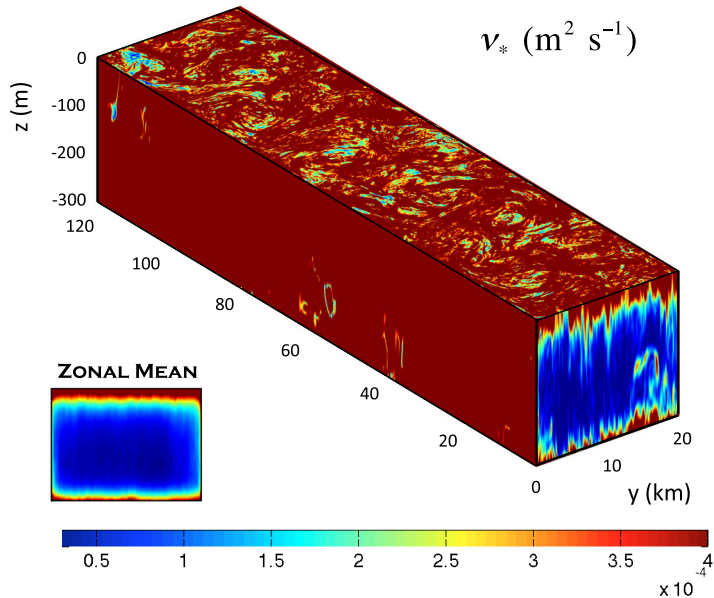


Figure 2. Snapshot of the QG Leith viscosity with limiter (55) is shown for a typical simulation, along with its along-channel mean (inset). Increased potential enstrophy and stratification variability in the upper and lower boundary layers increases the viscosity there (see Figure 4). Munk [1950] layers near the sidewalls form large relative vorticity gradients and thereby increase viscosity.

behavior in the salinity, temperature, and therefore buoyancy equation to handle D_{q_e} . The next section shows how this can be handled by way of Ertel potential vorticity conservation.

2.4.1. QG and Ertel Potential Vorticity

The equations (4)–(9) can be combined without approximation into vorticity and Ertel potential vorticity ($q_e = \omega \cdot \nabla(\bar{b} + b)$) budgets. For clarity and brevity, these equations are written in dimensional form in Cartesian index notation with Einstein summation and the z direction indicated by a z index. To avoid confusion, unlike in (4)–(9), the traditional approximation neglecting the horizontal component of planetary rotation is *not* made here, so the full planetary rotation 2Ω is used. These budgets are

$$\frac{D\omega_i}{Dt} = \partial_j [\omega_j u_i + \epsilon_{ijz} b + \epsilon_{i\ell k} \partial_\ell [D_v]_{jk}], \quad (41)$$

$$\frac{Dq_e}{Dt} = \partial_i [\omega_i \partial_j (\alpha_0 D_{0j} - \beta_S D_{Sj}) + \epsilon_{ij\ell} (\partial_k [D_v]_{jk}) \partial_\ell B], \quad (42)$$

$$\omega_i \equiv \epsilon_{ijk} \partial_j u_k + 2\Omega_i = -\epsilon_{ijk} \partial_j \epsilon_{kmn} \partial_m \Psi_n + 2\Omega_i. \quad (43)$$

The result uses the Levi-Civita contraction identity $\epsilon_{ijk} \epsilon_{kmn} = \delta_{im} \delta_{jn} - \delta_{in} \delta_{jm}$. Note that $\nabla_i \omega_i = 0$. Capital B is used to denote the total buoyancy, including the stratification, $B = (\bar{b} + b)$.

A broadly applicable form for the subgrid model stress tensor assumes a Boussinesq Newtonian fluid stress-resolved strain relation, $\tau_{jk} = v_{jkmn} (\partial_m u_n + \partial_n u_m)$, with a generic tensorial tracer flux-gradient relation, $D_{0j} = R_{jk} \partial_k \theta$ and $D_{Sj} = R_{jk} \partial_k S$. This flux-gradient relationship can include both an advective (antisymmetric) part and a diffusive (symmetric) part [Griffies, 1998], which allows for the standard mesoscale eddy tracer transport schemes [Gent and McWilliams, 1990; Redi, 1982] along with other similar closures [e.g., Fox-Kemper et al., 2008]. It will be assumed that all tracers are approximated to use the same coefficient tensor R_{jk} [Bachman and Fox-Kemper, 2013; Bachman et al., 2015].

$$\frac{D\omega_i}{Dt} = \partial_j [\omega_j u_i + \epsilon_{ijz} b + \epsilon_{i\ell k} \partial_\ell v_{jkmn} (\partial_m u_n + \partial_n u_m)], \quad (44)$$

$$\begin{aligned} \frac{Dq_e}{Dt} &= \partial_i [\omega_i \partial_j (\alpha_0 R_{jk} \partial_k \theta - \beta_S R_{jk} \partial_k S) + \epsilon_{ij\ell} (\partial_k v_{jkmn} (\partial_m u_n + \partial_n u_m)) \partial_\ell B], \\ &= \partial_i [\omega_i \partial_j (R_{jk} \partial_k B) + \epsilon_{ij\ell} (\partial_k v_{jkmn} (\partial_m u_n + \partial_n u_m)) \partial_\ell B]. \end{aligned} \quad (45)$$

If the diffusivity and viscosity are constant and isotropic, this becomes

$$\frac{Dq_e}{Dt} = \kappa \omega \cdot (\nabla^2 \nabla B) + v \nabla B \cdot (\nabla^2 \omega), \quad (46)$$

which is quite close to a dissipation of Ertel potential vorticity if $\kappa = v$. However, the goal here is to specify quasi-horizontal, or along-isopycnal eddy effects, those which control the cascade of potential enstrophy in horizontal scale and which are definitely not isotropic. For this, we consider the terms in square brackets in (45) one at a time.

The second term is the effect of viscosity on Ertel PV, and it is clear that it reverts to a term much like the one in (11) for barotropic flows when $\partial_i B$ is expected to point nearly along the gravitational direction. For other flows, homogenization of along-isopycnal velocities will lead to homogenization of Ertel PV. In the QG limit, where isopycnals are nearly flat, horizontal flow is nondivergent to leading order, and $N^2 \gg |\nabla_h b|$, the horizontal viscosity part of this term (which is the part predicted here) converges to $D_{q_2} N^2$, matching (18) in (16) aside from an overall dimensional constant N^2 .

The first term in square brackets in (45) is the effect of eddy diffusion (symmetric part of R_{jk} , or $S_{jk} = (R_{jk} + R_{kj})/2$) and eddy advection (antisymmetric part of R_{jk} , or $A_{jk} = (R_{jk} - R_{kj})/2$) on Ertel PV [Griffies, 1998; Bachman et al., 2015]. If, as argued by Redi [1982] and many others, eddy-induced diffusion is oriented along isopycnals, then $S_{jk} \nabla_k B = 0$, and there is no eddy diffusion of buoyancy [see also Dukowicz and Smith, 1997; Smith and Marshall, 2009; Abernathey et al., 2013] and thus no dissipation of Ertel PV by eddy diffusion in (45). If $S_{jk} \nabla_k B = 0$,

$$\frac{Dq_e}{Dt} = \partial_i [\omega_j \partial_j (A_{jk} \partial_k B) + \epsilon_{ij\ell} (\partial_k v_{jkmn} (\partial_m u_n + \partial_n u_m)) \partial_\ell B].$$

The A_{jk} may represent the Gent and McWilliams [1990] or another advective parameterization. Unlike diffusion, however, A_{jk} can affect PV dissipation without implying eddy-induced diapycnal fluxes. If eddy induced fluxes do not induce diapycnal fluxes, then $(\partial_j B) R_{jk} (\partial_k B) = (\partial_j B) A_{jk} (\partial_k B) = 0$. However, the advective fluxes may diverge meaningfully $\partial_j (A_{jk} (\partial_k B)) \neq 0$. That is, advective (a.k.a. skew) fluxes, $A_{jk} \partial_k B$, can affect buoyancy and PV even while oriented along isopycnals (i.e., $(\partial_j B) A_{jk} (\partial_k B) = 0$).

If we choose to follow the standard Gent and McWilliams [1990] eddy advection parameterization with a (scalar) transfer coefficient A_* , then the (pseudovector) stream function Ψ_k is proportional to the isopycnal slope,

$$\Psi_\ell = A_* \epsilon_{z\ell k} \frac{\partial_k B}{\partial_z B}, \quad (47)$$

$$A_{mn} = A_* \epsilon_{mnl} \Psi_\ell = A_* \epsilon_{mnl} \epsilon_{z\ell k} \frac{\partial_k B}{\partial_z B} = A_* \left(\delta_{nz} \frac{\partial_m B}{\partial_z B} - \delta_{mz} \frac{\partial_n B}{\partial_z B} \right). \quad (48)$$

Note that a z index implies the vertical direction only, and repeated z indices do not imply summation. If this form is used in (45) with constant A_* and a constant horizontal eddy viscosity v_* , the result is similar to (46)

$$\frac{Dq_e}{Dt} = A_* \omega \cdot (\nabla_h^2 \nabla B) + v_* \nabla B \cdot (\nabla_h^2 \omega) + \text{vert}, \quad (49)$$

$$\text{vert} = \partial_i \left(A_* \omega_i \partial_z \left[\partial_z B - \frac{|\nabla B|^2}{\partial_z B} \right] \right). \quad (50)$$

So, neglecting consequences of variations in A_* and v_* , consistent with the conversion from global to local in the derivation of the QG Leith coefficients, and accepting the cancellation in vertical terms in (50) as adequately small (i.e., $|\nabla B| \approx |\partial_z B|$), then $A_* = v_*$ is the optimal form for Ertel PV dissipation using the GM parameterization.

The distinction between advection and diffusion is not at all evident in the QGPV dissipation (16), because the geometry of quasi-geostrophic motions are asymptotically flattened by $N^2 \gg |\nabla_h b|$. Indeed, in QG, diffusivity of potential vorticity and tracers can be handled similarly, with a corresponding eddy Pe_* = Re_* producing dissipation of QG potential vorticity similar to (49) [see Fox-Kemper and Menemenlis, 2008]. However, the parameterization here must respect along-isopycnal physics in order to reduce spurious mixing. By using the along-isopycnal operators with QG predictions of the eddy coefficients, this along-isopycnal character is preserved in MOLES [Roberts and Marshall, 1998].

What about the specification of the Redi diffusivity, κ_* ? Dukowicz and Smith [1997] argue that a simple stochastic model where eddies simply rearrange parcels of fluid stochastically predicts that the GM coefficient and the Redi coefficient should be equal, $\kappa_* = A_*$ —at least when these coefficients do not vary vertically—again consistent with the Leith derivation's neglect of variations in coefficients.

It is possible to go a step farther, including vertical variations in the diffusivity according to *Smith and Marshall* [2009]. *Abernathay et al.* [2013] demonstrate that vertical variations can distinguish diffusivity of tracers (including potential vorticity) from the GM coefficient. They verify in simulations the *Smith and Marshall* [2009] result connecting the (vertically varying) GM coefficient A_* to the Redi tracer diffusivity κ_* ,

$$\partial_z \left(A_* \frac{\partial_k B}{\partial_z B} \right) = \kappa_* \partial_z \left(\frac{\partial_k B}{\partial_z B} \right) - \kappa_* \frac{\partial_y f}{f}. \quad (51)$$

The last term is expected to be only $O(\Pi_*)$, so quite small in MOLES applications. Equation (51) is consistent with the model of *Dukowicz and Smith* [1997] when the diffusivity varies in the vertical. If we now take the prediction of QG Leith to provide $v_* = \kappa_*$, then a version of A_* that depends on the entire water column can be formed from the definite integral of (51),

$$A_* \frac{\partial_k B}{\partial_z B} \Big|_{-H}^z = \int_{-H}^z \left(\kappa_* \partial_z \left(\frac{\partial_k B}{\partial_z B} \right) - \kappa_* \frac{\partial_y f}{f} \right) dz. \quad (52)$$

Using integration by parts and the fact that isopycnal slopes are very small at depth reveals the distinctions between A_* and κ_* ,

$$A_* \frac{\partial_k B}{\partial_z B} = \kappa_* \frac{\partial_k B}{\partial_z B} - \int_{-H}^z \left[\left(\frac{\partial_k B}{\partial_z B} \right) \partial_z \kappa_* - \kappa_* \frac{\partial_y f}{f} \right] dz. \quad (53)$$

Since (39) provides $v_* = \kappa_*$, all of the terms on the right side of (52) or (53) can be calculated, so this “corrected” form of the GM coefficient can be used in MOLES. Exploring this approach was not done for this work, only the simpler specification $v_* = \kappa_* = A_*$ is used. Note that many of the standard reasons not to use (53), such as rotational rather than downgradient PV fluxes [*Marshall and Shutts*, 1981; *Wilson and Williams*, 2004], integral constraints which are difficult to satisfy [*Killworth*, 1997], or spurious generation of motion [*Adcock and Marshall*, 2000], etc., are less relevant in the MOLES case where the largest eddies are resolved and therefore many of these eddy effects could be handled by resolved motions.

The arguments in this section only support using the GM and Redi diffusivity with the QG Leith closure. However, the next section will show how the 2-D Leith closure is often a good approximation of the QG Leith closure. As the 2-D Leith form is somewhat faster to calculate, one may opt to use the 2-D Leith viscosity from (32) along with $v_* = \kappa_* = A_*$.

2.4.2. Stability of the Vortex Stretching Term

The QG potential vorticity gradient in (39) and (40) differ from the 2-D vorticity gradient in (32) and (34) because of the vortex stretching term,

$$\nabla_h q_q = \nabla_h q_2 + \partial_z \frac{f}{N^2} \nabla_h b. \quad (54)$$

The N^2 in the denominator of the stretching term is an issue in numerical models where the flow is locally unstratified ($N^2 \rightarrow 0$) and the resultant large viscosities produced will lead to numerical instability.

When QG dynamics are relevant, (17) shows that the ratio of the relative vorticity gradient to the vortex stretching term in (54) is expected to be $\mathcal{O}(Bu_*)$. When the stratification is large, Bu_* is also expected to be large and the stretching term is expected to be small, so that the QG Leith viscosity (39) transitions toward the 2-D version (32). When the stratification is low, Fr_* is no longer small and the neglect of terms on the right-hand side of (16) to arrive at the QG Leith viscosity (39) must be reevaluated. Working through the scaling possibilities, a transition to 2-D Leith viscosity (32) is recommended when stratification gets too low.

A form for the viscosity that both contains the large Bu_* limiter and transitions into submesoscale dynamics by simply replacing large Fr_* with $Fr_* = 1$ in the small Bu_* limit is

$$v_* = \left(\frac{\Lambda \Delta s}{\pi} \right)^3 \min \left(\left| \nabla_h q_{2*} + \partial_z \frac{f^2}{N^2} \nabla_h b \right|, (1 + Bu_*^{-1}) |\nabla_h q_{2*}|, (1 + Ro_*^{-2}) |\nabla_h q_{2*}| \right). \quad (55)$$

This form is sufficient for the simulations here where no mixed layer is present. In the presence of a mixed layer or convection, the 2-D theory (32) is used to represent barotropic dynamics wherever the boundary layer mixing scheme is active. In submesoscale-resolving simulations, where even the mixed-layer deformation radius is resolved, it is possible that this limiter will suffice without reversion.

An alternative form of (55) which smoothly transitions to the 2-D limit for $\text{Fr}_* \geq \mathcal{O}(1)$ is

$$v_* = \left(\frac{\Lambda \Delta s}{\pi} \right)^3 \sqrt{\min \left(|\nabla_h q_{2*} + \partial_z \frac{f^2}{N^2} \nabla_h b|, \left(1 + \frac{\text{Fr}_*^2}{a_R \text{Ro}_*^2 + \text{Fr}_*^4} \right) |\nabla_h q_{2*}| \right)^2 + |\nabla [\nabla \cdot \mathbf{v}_h]|^2}. \quad (56)$$

A tunable parameter a_R is provided for flexibility, but a value of 1 is adequate.

A limiter is important for numerical stability of the simulations in section 3. A tapering scheme is still required to accommodate the calculation of GM and Redi terms at steep slopes [e.g., Aiki *et al.*, 2004; Ferrari *et al.*, 2008, 2010]. However, in MOLES the majority of the tracer transport is done by resolved eddies which are not tapered.

2.5. Subgrid Models for Generalized 2-D Turbulence

Generalized 2-D turbulence [Pierrehumbert *et al.*, 1994] includes 2-D turbulence, large-scale QG (LQG) turbulence [Larichev and McWilliams, 1991] and surface quasi-geostrophic (SQG) turbulence [Blumen, 1978; Held *et al.*, 1995; Lapeyre and Klein, 2006; Tulloch and Smith, 2006], among other flow types that rely on relationships between stream function and vorticity [e.g., Callies *et al.*, 2016]. Salmon [1978] extends QG theory to consider the combined effect of both barotropic and baroclinic components on turbulent cascades. Following Charney [1971], boundary effects are neglected here in the formulation of the QG Leith model. All of these theories are solved using an equation, or set of equations for multiple layers, that resemble (11), but with $\hat{q} = -\mathbf{k}^\alpha \hat{\psi}$. Smith *et al.* [2002] derive spectral cascade theories for many choices of α .

However, not all of these are useful in the way that QG and 2-D turbulence are useful here for using D_q to infer deterministic subgrid models suitable for 3-D MOLES. Inverse cascades are interesting, but subgrid models for inverse cascades are not particularly meaningful in the absence of backscatter or stochastic forcing to generate the cascaded variability at the gridscale. The Smagorinsky viscosity (23) works as a halt on the 2-D or QG inverse energy cascade, but it is strange to contemplate because the energy should be generated at the gridscale and cascaded to larger scales. Jansen and Held [2014] propose a scheme roughly along these lines. Furthermore, the oceanic inverse cascade is halted on scales just slightly above the injection scale [Arbic and Flierl, 2004; Scott and Wang, 2005; Thompson and Young, 2007] while the atmospheric inverse cascade is limited by the size of Earth [Chemke and Kaspi, 2015]. Baroclinic instability injects variance near the deformation radius, so natural systems will have inverse cascades on scales larger than the deformation radius and direct cascades on smaller scales. LQG requires even its forward cascade to occur on scales *larger* than the deformation radius, thus the LQG forward cascade is not realized in earth's ocean and atmosphere. The direct available potential energy cascade of SQG [Blumen, 1978] can be used to derive a horizontal diffusivity following the approach above, $\kappa_* = (\Gamma \Delta s / \pi)^2 \sqrt{|\nabla b_*|}$, for a constant tuning parameter Γ . The cascade in SQG concerns only the available potential energy on bounding surfaces or PV sheets [Callies *et al.*, 2016], thus this estimate only provides a diffusivity at the bounding surface and not the interior values needed for 3-D MOLES.

2.6. Planetary Curvature

One expects that the resolved fluid stirring will tend toward straining and then homogenization [Rhines and Young, 1982] of the absolute vorticity rather than the relative vorticity. Thus, the vorticity gradients relevant to the generalized enstrophy cascades are expected to include variations in the vorticity due to the planetary curvature, as in (11) and (16). However, the contributions from the planetary vorticity gradient to the viscosity are expected to be small $\mathcal{O}(\text{Pl}_*/\text{Ro}_*)$, and anisotropy and jet formation will tend to be *resolved* in MOLES rather than provided through the closure as in coarse resolution models. As the meridional gridscale is always significantly smaller than the radius of the earth, $\text{Pl}_* \leq \mathcal{O}(10^{-2})$ except very near the equator. Indeed, the idealized simulations here were run on an *f*-plane, neglecting these effects entirely. Effectively, the β term in the 2-D and QG Leith schemes will provide a minimum viscosity in quiescent regions.

2.7. Dissipation Operators for Primitive Equations

The viscosity and diffusivity for subgrid models in 2-D and QG dynamics have been based on approximations of the true dissipation operators that result when the curl of the 3-D momentum equation is taken or a standard derivation of QG is followed [Pedlosky, 1987; Vallis, 2006]. However, in 3-D MOLES, it is not desirable to retain these approximated dissipation operators, as these violate conservation principles of the original 3-D MOLES equations. Instead, only the scaling for the coefficients—viscosity and diffusivity—are

brought back from the QG theory to the 3-D equations, *not* the whole dissipation operator. By this approach, the dissipation in the 3-D equations continues to respect angular momentum, momentum, and tracer conservation, but the viscosities in the horizontal plane are provided by (39) or (32).

As (39) and (32) are quite similar in many circumstances, and (32) is computationally less expensive to calculate, using the (32) estimate as a GM/Redi coefficient may be an adequate approximation. Unlike the PV dissipation argument above, no theory relates the 2-D scaling to GM/Redi coefficient or diffusivity, except the similar spatial patterns of QG Leith and 2-D Leith.

Oftentimes, biharmonic or even higher differential orders are chosen in high-resolution simulations, to make diffusion highly scale selective. However, flow-aware schemes can be as scale-selective and even more selective of anomalous small-scale events than higher derivatives. However, because of the common use of biharmonic operators in ocean models, the new schemes proposed here are contrasted against common biharmonic operators. Griffies and Hallberg [2000] and Fox-Kemper and Menemenlis [2008] show that a biharmonic viscosity of $\nu_{4*} = \Delta s^2 \nu_* / 8$ can be used to come close in effect to a harmonic viscosity. This relationship can be used to form biharmonic forms of the 2-D Leith and QG Leith schemes.

The viscosity, diffusivity, and eddy-induced advection here can all be used in high-resolution models regardless of vertical coordinates. Some care is needed to make appropriate coordinate thickness weighting [de Szoeke and Bennett, 1993; Young, 2012].

2.8. The Dynamical Model

The notion of building a SGS model is based on the LES approach to numerically solving the Navier-Stokes equations, which is that the numerical solution is a filtered version of the true solution. The gridscale itself is a filter (denoted here by an asterisk), but in the dynamical model an additional explicit low-pass “test filter” at a scale $\alpha \Delta s$ larger than the grid filter scale Δs (denoted here with an overbar) is used for the dynamical adjustment of the viscous coefficient. Dynamical subgrid models have a long history in LES [Germano *et al.*, 1991; Lilly, 1992; Meneveau *et al.*, 1996; Meneveau and Katz, 2000], and are typically used in 3-D isotropic turbulence to dynamically adjust the coefficient of the Smagorinsky [1963, 1993] viscosity, Υ in (23).

The same concept can be applied to the QG Leith viscosity, that is, the filtered, resolved stresses can be used to calculate a consistency relation that determines the Leith coefficient Λ . Central to this concept is the Germano [1992] identity, a tautological constraint which relates the explicitly filtered Leonard [1974] stress, L , to the filtered subgrid model stress, $\overline{\tau}$,

$$L_{ij} = \overline{(u_i u_j)_*} - \overline{u_{*i}} \overline{u_{*j}} + \overline{\tau_{*ij}}. \quad (57)$$

Fox-Kemper and Menemenlis [2008] show that the Germano identity applied to Leith viscosity is

$$L_{ij} - \frac{1}{3} L_{kk} \delta_{ij} = \left(\frac{\Lambda}{\pi} \right)^3 M_{ij}, \quad (58)$$

$$M_{ij} = \left(\alpha \Delta s |\nabla_h q_{q*}| \frac{1}{2} \left(\frac{\partial u_i}{\partial x_j} + \frac{\partial u_j}{\partial x_i} \right) - \Delta s |\nabla_h q_{q*}| \frac{1}{2} \left(\frac{\partial u_i}{\partial x_j} + \frac{\partial u_j}{\partial x_i} \right) \right), \quad (59)$$

$$\Lambda = \pi \left[\frac{\langle L_{ij} M_{ij} \rangle}{\langle M_{ij} M_{ij} \rangle} \right]. \quad (60)$$

The $\langle \cdot \rangle$ brackets indicate an averaging operation, without which the dynamic model yields highly variable and potentially negative viscosities [Lilly, 1992; Liu *et al.*, 1995] which often crash the model. A variety of such averaging operations have been attempted [Piomelli, 1993; Piomelli and Liu, 1995; Meneveau *et al.*, 1996] which require at least one statistically homogeneous direction, as well as other more general models which do not require a homogeneous direction [e.g., Ghosal *et al.*, 1995]. It is very unlikely that sophisticated and expensive averaging schemes can be afforded (or arguably needed) if a dynamic model is attempted in an oceanic GCM, so simplicity is favored. Therefore, the averaging used follows Ghosal *et al.* [1995], where the viscosities are simply constrained to be nonnegative and then locally averaged for smoothing.

Test filtering is easy in a spectral model where scales are isolated in spectral regions already. Most common filters are equivalent to convolutions between a model field and a filter kernel as in (57), which are

inexpensive and accurate in spectral models. Near spectral accuracy is achievable with large-stencil filters in physical space, but they are expensive in the brute force implementations that are most natural for OGCM discretizations and irregular coastlines. Smaller 3-point or 5-point stencils are affordable but limited in accuracy.

For the idealized simulations in this study a fourth-order discrete box filter is employed [Sagaut and Grohens, 1999]. This filter has the advantages that it uses a compact stencil (5 points) is simple to employ in a nonspectral code and is derived using Taylor expansions, meaning it could be modified straightforwardly for use on a nonuniform mesh. The filtering operation in one dimension on a variable ϕ is defined by

$$\bar{\phi} = \frac{3\gamma^4 - 20\gamma^2}{5760}(\phi_{i+2} + \phi_{i-2}) + \frac{80\gamma^2 - 3\gamma^4}{1440}(\phi_{i+1} + \phi_{i-1}) + \frac{3\gamma^4 - 100\gamma^2 + 960}{960}\phi_i, \quad (61)$$

for a grid index i . The free parameter $\gamma = \bar{\Delta s}/\Delta s$ is the ratio of the targeted test filter scale to the grid scale. For discrete test filters this γ is convertible, but not equal, to the scaling factor α as defined in (59) [Vreman, 1995; Najjar and Tafti, 1996; Lund, 1997]. For example, setting $\gamma = 2$ in the fourth-order box filter corresponds to $\alpha = \sqrt{6}$, which is the value used in the computation of (59). A multidimensional version of this filter can be formed by applying (61) sequentially in the x direction first, and then in y .

3. Simulation Results and Discussion

A series of frontal spin-down simulations are used to test both the basic QG Leith scheme with a preset coefficient, and the dynamic scheme where the coefficient is calculated at every time step. The same simulations are repeated with other commonly employed viscosity schemes (2-D harmonic Leith, 2-D biharmonic Leith, harmonic Smagorinsky, biharmonic Smagorinsky, harmonic constant coefficient, and biharmonic constant coefficient). Only the QG Leith schemes use the GM/Redi parameterization—all other schemes specify horizontal viscosity only. All simulations use a third-order upwinding scheme for the tracer equations, which ensures stability and dissipation of tracers according to numerical (not physical) specifications. In the simulations using the GM parameterization a simple vertical tapering is used [Large et al., 1997] to ensure that there is no buoyancy flux through the vertical boundaries.

The hydrostatic, Boussinesq equations are solved using the MITgcm [Marshall et al., 1997] to simulate a zonally reentrant channel with a temperature front oriented in the cross-channel direction that extends from the free surface to the bottom boundary, akin to the Eady [1949] model. In these simulations all viscous boundary conditions are slip, and the velocity fields are initialized in geostrophic balance to minimize ageostrophic waves. The initial stratification is independent of the along-front direction. To simulate QG dynamics with interesting vortex stretching, both the horizontal and vertical buoyancy gradients, M^2 and N^2 , are made to vary with depth. Setting the geostrophic Richardson number, $Ri = N^2 f^2 / M^4 = 50$ at all depths, expressions for the stratification parameters can be written

$$N^2 = Ri f^2 (1 + 0.8 \frac{z}{H}) \text{ s}^{-2}, \quad (62)$$

$$M^2 = \left(\frac{N^2 f^2}{Ri} \right)^{1/2} \text{ s}^{-2}, \quad (63)$$

$$\bar{b}(y, z) = b_0 + \int_{-H}^z N^2 + \frac{\Delta s M^2}{2} \tanh \left[\frac{2(y - y_0)}{\Delta x} \right] dz, \quad (64)$$

where $H = 300$ m is the total depth, $f = 7.29 \times 10^{-5} \text{ s}^{-1}$, and Δs is the (isotropic) grid spacing. With these parameters N^2 and M^2 vary between $5.4 \times 10^{-8} \text{ s}^{-2}$ and $2.4 \times 10^{-9} \text{ s}^{-2}$ at the bottom, respectively, and $2.7 \times 10^{-7} \text{ s}^{-2}$ and $5.3 \times 10^{-9} \text{ s}^{-2}$ at the top.

Note that L_d and H are small for typical “mesoscale” values and fall into more “submesoscale” values. However, great care has been taken to appropriately choose the dimensionless parameters which are the real distinction between these regimes, where we define the mesoscale regime to be where $Ro \ll 1$ and $Fr \gg 1$, and the submesoscale to be where $Ro \sim 1$ and $Fr \sim 1$. Using a thermal wind scaling $V_* \sim M^2 H / f$ with the mean value of M^2 gives a typical velocity scale of 0.01 m s^{-1} , and by (2) the first deformation radius is $L_d = 512$ m. Then at the deformation radius,

$$\text{Ro} = \mathcal{O}(10^{-1}), \quad \text{Fr} = \mathcal{O}(10^{-1}), \quad \text{Bu} = \mathcal{O}(1), \quad (65)$$

and at the gridscale (which ranges between $0.1L_d \approx 50$ m and $2L_d \approx 1000$ m),

$$\text{Ro}_* = \mathcal{O}(10^{-1}) \text{ to } \mathcal{O}(1), \quad \text{Fr}_* = \mathcal{O}(10^{-1}), \quad \text{Bu}_* = \mathcal{O}(1) \text{ to } \mathcal{O}(100). \quad (66)$$

Quasi-geostrophic dynamics, characterized by $\text{Ro}_* \ll 1$, $\text{Fr}_* \ll 1$, and $\text{Bu}_* = \mathcal{O}(1)$, are at least marginally applicable in all simulations.

The initial conditions are held fixed across all simulations, but to quantify scale-awareness and flow-awareness, each subgrid scheme is simulated with a hierarchy of five simulations differing in grid resolution. Three sets of simulations are run where Δs is smaller than L_d by a factor of 2.5, 5, and 10 (corresponding to $\text{Bu}_* = 6, 25$, and 100, respectively). These three choices of Δx all permit and increasingly resolve the forward potential enstrophy cascade regime where the QG Leith scheme is designed to be optimal. These resolutions resemble those in forthcoming generations of GCMs, where an enstrophy cascade is prevalent but the inertial range may be limited. The last two simulation sets are conducted with the grid spacing equal to and greater than L_d , so that $L_d = \Delta s, \text{Bu}_* = 1$ and $2L_d = \Delta s, \text{Bu}_* = 1/4$. These simulations are designed to test the schemes when the forward enstrophy cascade is not permitted. However, (weak) eddies still form even at these coarse resolutions.

Soon after initialization the front undergoes slumping by baroclinic instability, which grows by extracting mean potential energy from the background flow. This has the effect of tilting the mean isopycnals as shown in Figure 3. The simulations are run until just before the edge of the front reaches the lateral wall. The simulations are stopped at this point to avoid contamination or wave reflection from the lateral boundary. Statistics are taken at the end of the simulation, when the energy and enstrophy spectra have fully developed and have well-defined slopes. To be consistent, all simulations are run for and analyzed at the same total dimensional time. Because the fastest-growing baroclinic modes are most well-resolved in the $L_d = 10\Delta s$ simulations, the highest resolution runs reach the lateral boundary first, setting the run and analysis time for all simulations. The lower-resolution simulations do not slump as far and thus also avoid boundary effects. The kinetic energy of the coarsest runs is weaker even at large scales, reflecting their inefficient extraction of potential energy during the allotted time. Nonetheless, all simulations have spectra that are well-defined by the designated simulation stopping time.

In physical space, because of the symmetry of the scenario the structures of both the kinetic energy (Figure 4a) and potential enstrophy (Figure 4b) are fairly uniform across the domain. However, smaller scale variations in potential enstrophy indicate the shallow spectral slope of this field and its forward cascade, while the steeper spectral slope and inverse cascade of kinetic energy leads to only a few dominant features.

The experiments run at $L_d = 2.5\Delta s$ roughly correspond to the resolution anticipated in the next generation of climate-scale GCMs (roughly $1/6^\circ$ Mercator equivalent at $30^\circ S$ and $30^\circ N$ and based on Hallberg [2013]). The simulations at $L_d = 10\Delta s$ correspond in the ocean to the transition between mesoscale and submesoscale dynamics (roughly $1/25^\circ$ Mercator at $30^\circ S$ and $30^\circ N$), where the Rossby number is $\mathcal{O}(1)$ and the assumptions of QG dynamics begin to break down. Of course, at these high resolutions, the subgrid scheme has very little effect on lengthscales near L_d . The coarser runs at $L_d = \Delta s$ and $2L_d = \Delta s$ correspond to global runs that are barely eddy permitting (0.4° and 0.8° at $30^\circ N$), such as those that are laminar in the extratropics.

These simulations do not include parameterizations or forcing of any smaller-scale processes such as Langmuir turbulence [e.g., McWilliams *et al.*, 1997; McWilliams and Sullivan, 2000] or submesoscale mixed-layer instability [Fox-Kemper *et al.*, 2008], so the spectra at all depths are expected to be dominated by the QG dynamics. The study of other effects, such as transitions across the equator or deep convection, is left to future work.

Figure 5 compares the average viscosity that results in the different simulations with different resolutions and subgrid models. 2-D Leith tends to have the lowest average viscosity, while Smagorinsky tends to have the largest. QG Leith is systematically larger than 2-D Leith, revealing that the stretching term tends to be an important additive effect in (54).

The subgrid models are fundamentally different. Note that while each of the nonlinear subgrid models in Figure 5 have a tunable parameter (Υ, Λ) their average viscosities differ by about three orders of

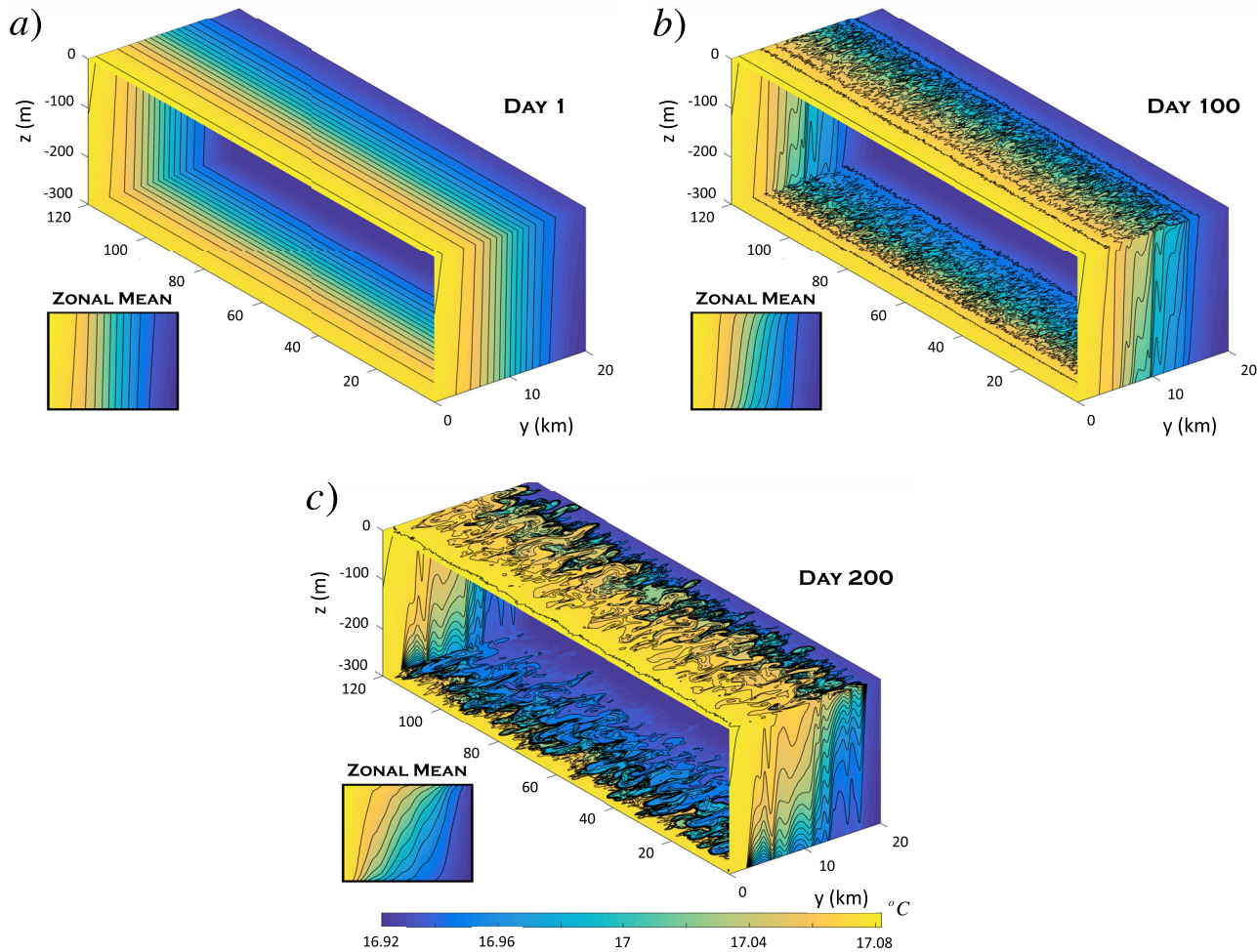


Figure 3. Typical model snapshots of potential temperature for the frontal spin-down configuration described in section 3. (a) The model is initialized with linear functions of z for M^2 and N^2 , so that at each level $Ri = 50$. (b) The flow is unstable to baroclinic instability, which grows at the expense of the mean potential energy of this density profile. (c) The simulation is halted before the front reaches the lateral wall. Although locally the potential temperature profile is noisy, in the along-channel mean the systematic slumping is evident (insets).

magnitude, and their slopes of increase with increasing Δs do not agree. The theory predicts that these tunable parameters should be $\mathcal{O}(1)$, but tuning them to agree in average viscosity would require retuning Υ and Λ by roughly an order of magnitude. Even if they were tuned to agree on average at one particular Δs , they would not agree at other choices of Δs . Furthermore, as these subgrid schemes are flow-aware based on different flow variables (D_* , $\nabla_h q_{2*}$, $\nabla_h q_{q*}$), even if their average values agree they would not agree pointwise.

As resolution changes, the viscosity is scaled according to standard practice for each subgrid scheme. We can estimate the scaling of viscosity with gridscale for each subgrid model if the dynamics are dominated by an enstrophy or potential enstrophy cascade ($E \propto \eta^{2/3} k^{-3}$, $G \propto \eta^{2/3} k^{-1}$). If the feedback of viscosity onto the production of energy and enstrophy is ignored and the inertial range theory is assumed, then dimensional analysis results in $v_* \propto \Upsilon^2 \eta^{1/3} \Delta s^2$ for Smagorinsky and $v_* \propto \Lambda^3 \eta^{1/3} \Delta s^2$ for Leith. However, Figure 5 shows that the volume-averaged viscosity differs in practice from these scalings with resolution, because the inertial range is imperfectly realized (i.e., factors such as k_p/k_* contribute), excessive damping or underdamping changes the potential enstrophy production rate η , and the coarsest two resolutions do not permit a potential enstrophy cascade. The QG Leith results scale nearly according to $v_* \propto \Delta s^2$ for higher resolution runs, while the 2-D Leith results follow a steeper scaling ($v_* \propto \Delta s^{2.5}$) and the Smagorinsky models follow a shallower ($v_* \propto \Delta s^{1.8}$) scaling. The constant harmonic and biharmonic viscosities are tuned by adjusting a combination of the model time step and a dimensionless prefactor so that these scale precisely as Δs^2 .

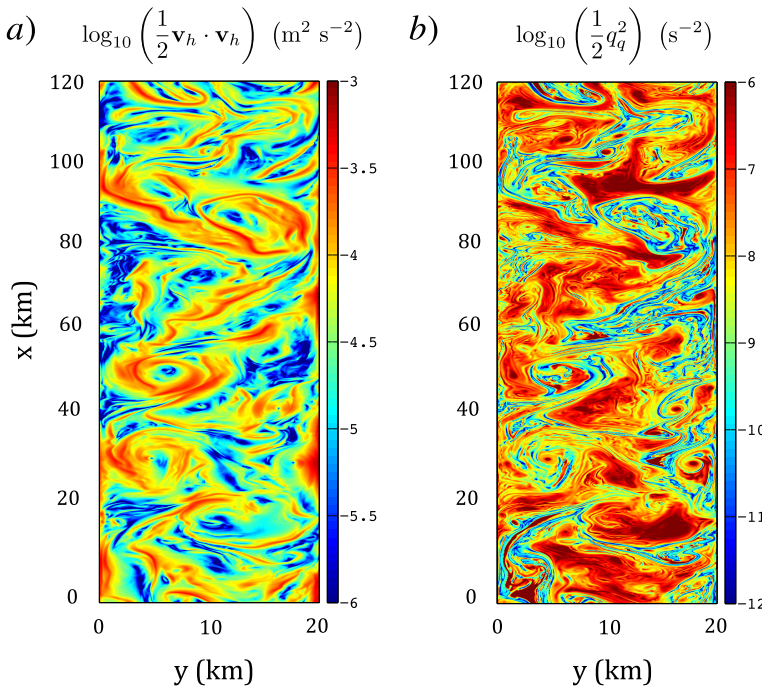


Figure 4. Base-10 logarithm of surface (a) kinetic energy ($\mathbf{v}_h \cdot \mathbf{v}_h / 2$) and (b) potential enstrophy ($q_q^2 / 2$) from the same simulation as Figure 3 at Day 200.

Figures 6 and 7 show the energy and enstrophy spectra for all simulations. Colors are chosen by resolution. Red is the coarsest simulation, green is next, the blue simulations span the “eddy-rich” regime, and black is the highest-resolution simulation. The dashed line indicates the anticipated spectral slope for each variable in the forward cascade regime, which is -3 for energy and -1 for potential enstrophy. The range of spectra from the highest-resolution QG Leith, 2-D Leith, harmonic and biharmonic simulations are indicated by the gray shaded area, and are to be interpreted as a multimodel “truth” against which the coarser-resolution experiments can be compared. The Smagorinsky experiments are excluded from the multimodel ensemble

due to their obvious deviation away from the dashed line. All of the spectra within each sub-panel share the same subgrid scheme, scaled according to the preceding formulae.

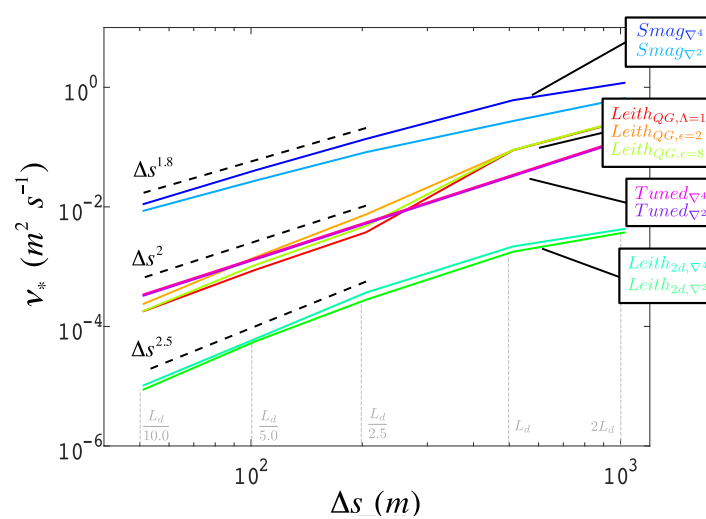


Figure 5. A wide range for average viscosity (ν_*) results from using the different closures as a function of horizontal resolution (Δs). Biharmonic viscosities are shown here using the conversion factor $\nu_{2*} \approx \nu_{4*} \cdot 8 / \Delta s^2$ [Griffies and Hallberg, 2000; Fox-Kemper and Menemenlis, 2008]. The label above each dashed black line is its slope, which shows how the viscosity scales with resolution. The dashed gray lines indicate the resolution at which each simulation was run.

The central result in the energy spectra in Figure 6 is that in all simulations at eddy-rich resolutions and finer (blue) both the fixed parameter form of QG Leith viscosity (where $\Lambda = 1$) and the dynamical form with filter width $\epsilon = 8$ maintain an approximately k^{-3} spectral slope of energy all the way to the grid-scale—closely matching the multimodel “truth” (gray shaded area). In the simulations where the gridscale lies above the deformation radius all versions of Leith viscosity yield a $-5/3$

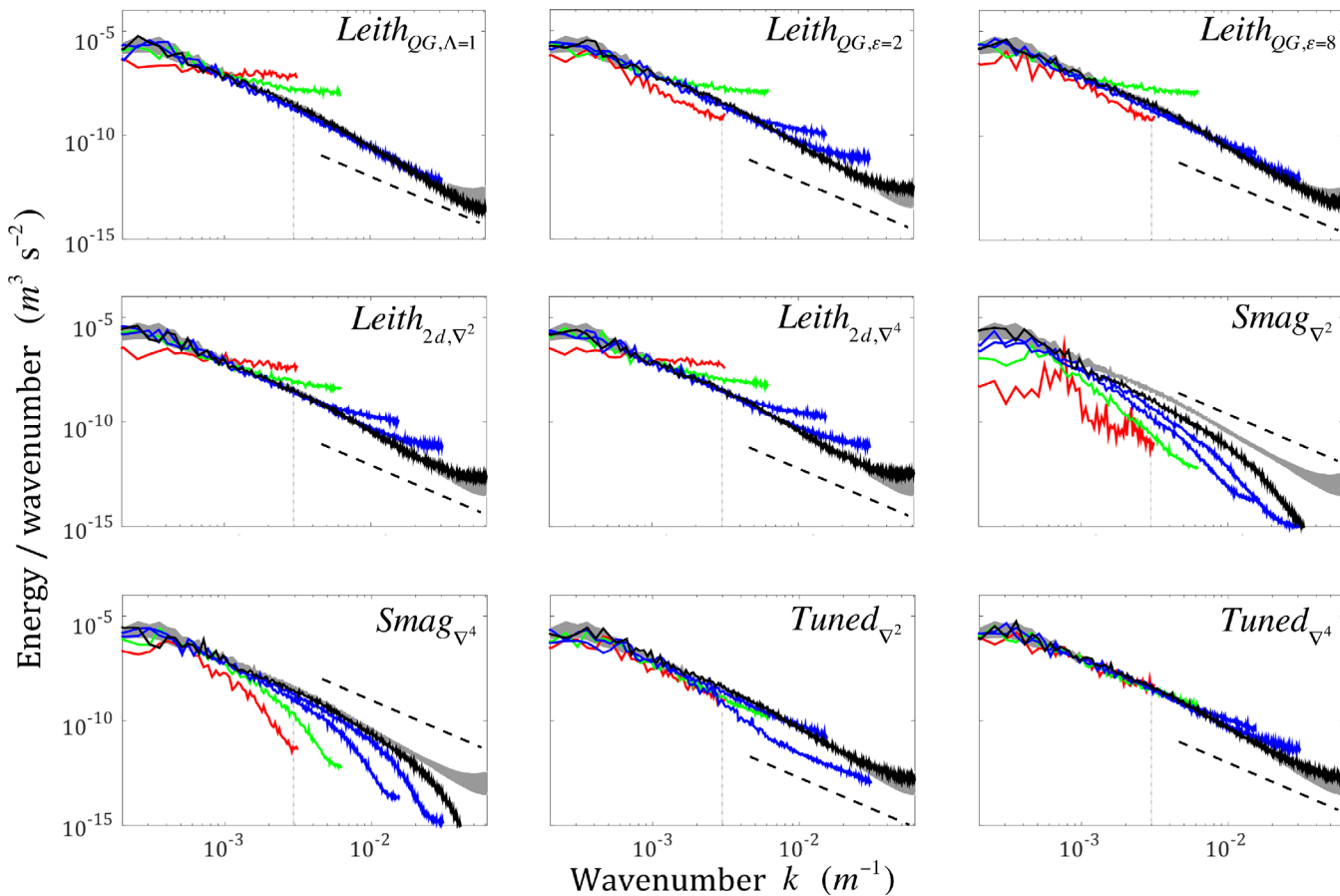


Figure 6. Energy spectra for the simulations where the deformation radius is explicitly resolved, decreasing in resolution from $\Delta s=L_d/10$ (black), $\Delta s=L_d/5$ (blue), $\Delta s=L_d/2.5$ (blue), $\Delta s=L_d$ (green), to $\Delta s=2L_d$ (red). The dashed black lines show the k^{-3} spectral slope of energy anticipated by theory in the LSQG forward potential enstrophy cascade regime. The gray shaded area represents “truth,” which is the range of spectra covered by the highest-resolution simulations excluding Smagorinsky. Subpanels indicate the results for simulations using different subgrid schemes: (top left) QG Leith, $\Lambda_q=1$, (top center) dynamic QG Leith, filter width $=2\Delta s$, (top right) dynamic QG Leith, filter width $=8\Delta s$; (middle left) harmonic 2-D Leith, $\Lambda_2=1$, (middle center) biharmonic 2-D Leith, $\Lambda_4=1$, (middle right) harmonic Smagorinsky $\Upsilon_2=3.0$; (bottom left) biharmonic Smagorinsky, $\Upsilon_4=3.0$, (bottom center) constant harmonic, $v_2=\Delta s^2/\Delta t$, (bottom right) constant biharmonic, $v_4=\Delta s^4/\Delta t$. Vertical line indicates approximate fastest growing instability wave number of $2\pi/3.9L_d$. The spectra are measured at the simulation stopping time, which occurs before the edge of the front reaches the lateral boundary.

slope, in agreement with Large Scale QG (hereafter LSQG) as found by *Smith et al.* [2002]. These slopes are also in agreement with observations by *Le Traon et al.* [2008], who found the sea surface height spectra to follow $k^{-11/3}$, which would imply a KE slope of $k^{-5/3}$. They argued this is SQG, not large-scale QG, but both are consistent.

The energy spectral performance of the dynamically prescribed QG Leith viscosity (Figure 6, top) is dependent on the filter width ϵ , consistent with previous studies on dynamical filters [e.g., *Najjar and Tafti*, 1996]. In these simulations a wider test filter ($\epsilon=8$) reproduces the correct spectra more closely than the narrow filter ($\epsilon=2$), in contrast with previous studies which have found little sensitivity to the choice of ϵ [*Lund*, 1997]. Nonetheless, the performance by simply setting $\Lambda=1$ rivals that of the most expensive, large-stencil filter and suggests that the extra computation cost of the dynamical scheme will outweigh its potential benefits when used in a GCM. Avoiding the additional complexity of designing filters for use with complex topography is a beneficial side benefit.

By contrast, both harmonic and biharmonic forms of the 2-D Leith viscosity underdamp energy (Figure 6, middle row, left and center column) and are noisy at small scales with spectral slopes that are too shallow and not in agreement with QG (or 2-D) theory. This underdamping is symptomatic of the difference between the potential enstrophy cascade in these simulations and the enstrophy cascade that is assumed in the 2-D Leith theory. Note that this underdamping persists even though Bu_* is quite large, and thus the modest differences between 2-D and QG Leith are significant even at high resolution.

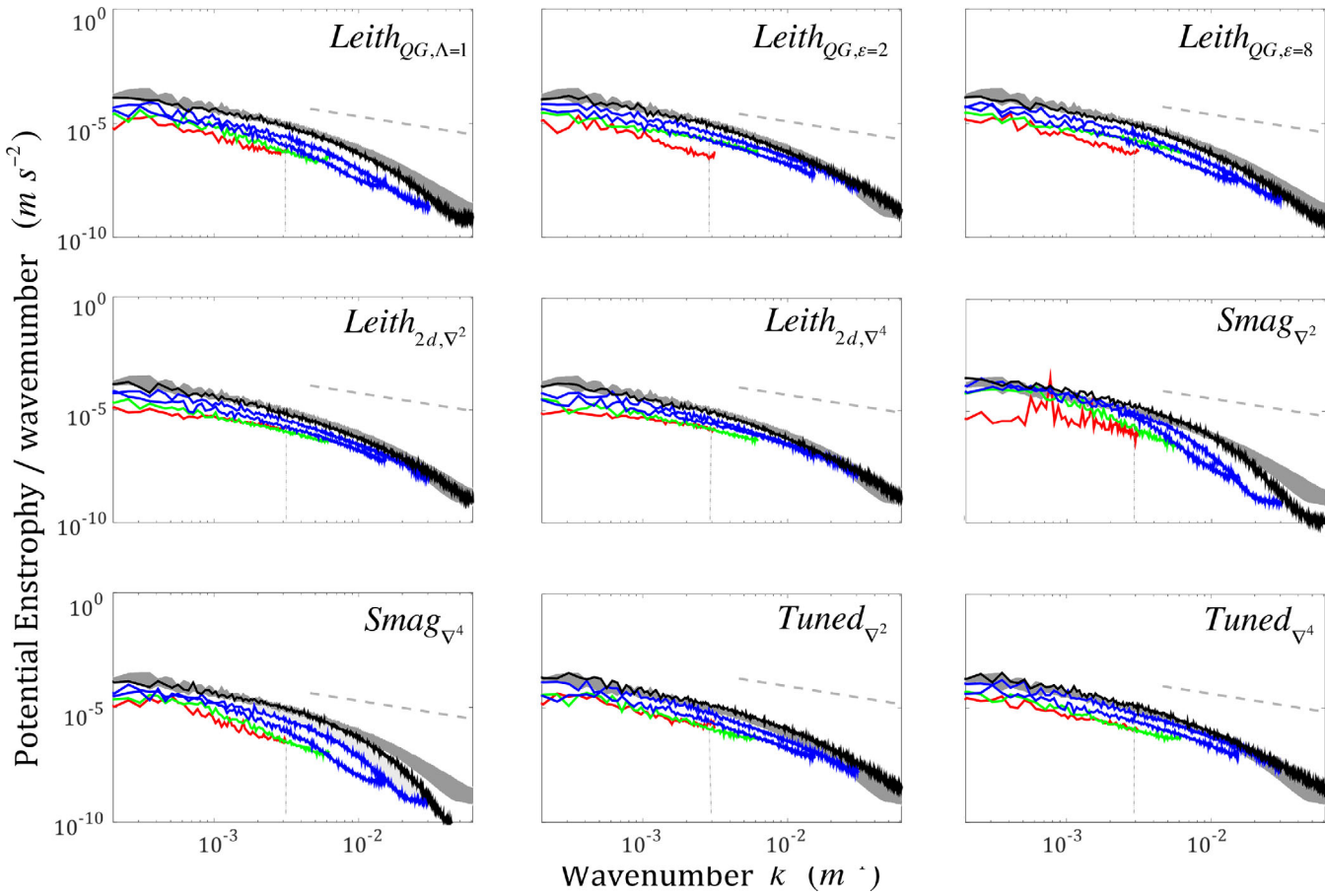


Figure 7. Potential enstrophy spectra for the simulations where the deformation radius is explicitly resolved, decreasing in resolution from (a) $L_d = 10\Delta s$, (b) $L_d = 5\Delta s$, to (c) $L_d = 2.5\Delta s$. The dashed gray lines show the k^{-1} spectral slope of potential enstrophy anticipated in the forward cascade regime. The gray shaded area represents “truth,” but in this case even the “truth” runs are likely contaminated by numerics (see Figure 8). Subpanels indicate the results for simulations using different subgrid schemes, and are arranged as in Figure 6. Vertical line indicates approximate fastest growing instability wave number of $2\pi/3.9L_d$. The spectra are measured at the simulation stopping time, which occurs before the edge of the front reaches the lateral boundary.

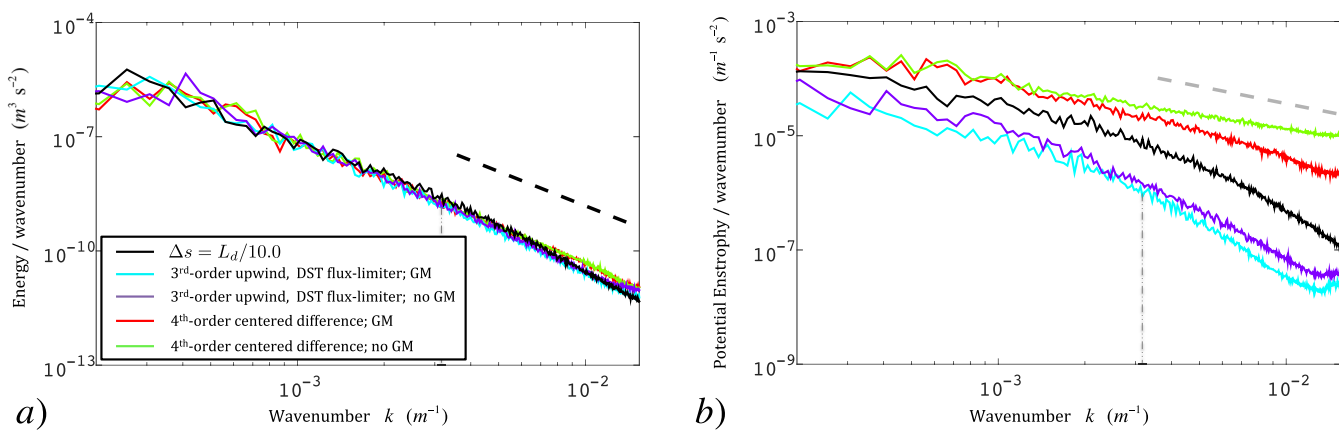


Figure 8. (a) Energy spectra and (b) potential enstrophy spectra for simulations using QG Leith but differing in tracer advection scheme (diffusive third order upwind versus nondiffusive fourth order centered difference) and whether or not the GM/Redi eddy-induced isoneutral diffusion and advection are used. Background diapycnal diffusion is held fixed across the simulations. The black line indicates the highest resolution QG Leith result from Figures 6 and 7. The dashed black line in Figure 8a depicts the predicted k^{-3} spectral slope of energy, and in Figure 8b the dashed gray line depicts the k^{-1} spectral slope of potential enstrophy.

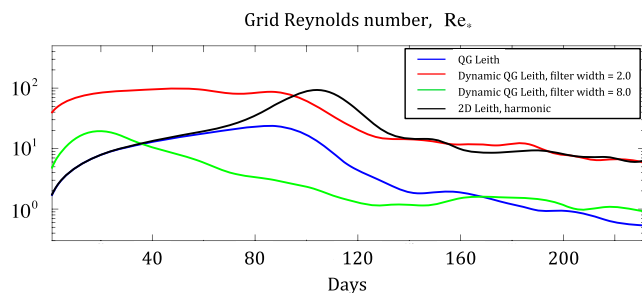


Figure 9. Grid Reynolds number $Re_* = V_* \Delta s / v_*$ for simulations with $L_d = 5\Delta s$ and using either harmonic 2-D Leith or QG Leith viscosity. The 2-D Leith and QG Leith ($\epsilon = 2$) viscosities are not sufficiently dissipative and yield $Re_* > 1$. For the $\Lambda = 1$ and $\epsilon = 8$ QG Leith simulations, after the initial spin-up is complete and the spectra become well-resolved Re_* asymptotes to one for the duration of the simulations.

Finally, the simulations with constant coefficient viscosity, both harmonic and biharmonic, maintain approximately k^{-3} spectral slopes of energy down toward the gridscale, and reproduce “truth” nearly as well as the Leith schemes at high resolution. They outperform all subgrid models at the coarsest resolutions, lauding the standard practice of using scale-aware, but constant viscosity in RANS. However, extensive tuning was required for these simulations to yield the desired quality, as each viscosity is dependent on both the grid resolution and time step ($v_* = \Delta s^2 / \Delta t$ for harmonic, and $v_* = \Delta s^4 / \Delta t$ for biharmonic). Four times as many simulations were needed for each case to adjust the viscosities to be of the comparable magnitude to the nonlinear schemes (Figure 5), or equivalently about half of the total computing time was spent on readying these two of the nine subgrid schemes. Only after this detailed tuning exercise were these correct energy spectral slopes with minimal roll-off manifested, and prior knowledge of the model velocity fields and decay timescale was needed to inform the tuning. By contrast, the Leith schemes performed optimally on the first try with no tuning required. The idealization of these models, with simplistic stratification and domain boundaries permits a homogeneous eddy field, which significantly, and unrealistically, aids the tuning of constant viscosities. In realistic ocean models the viscosities would need to vary spatially.

The enstrophy spectra are similarly variable, but none of the subgrid models is able, using the present numerics, to capture the theoretical slope (k^{-1}) all the way to the gridscale. The QG and 2-D Leith schemes outperform the Smagorinsky schemes, but there is room for improvement in all cases. Three possible hypotheses for this mismatch are: (1) that the numerical upwinding scheme is dissipating too much potential enstrophy near the gridscale—beyond what theory requires, (2) that a potential vorticity damping scheme might be more consistent with the QG theory than GM/Redi, or (3) that the model’s imperfect conservation of potential vorticity leads to error.

The consequences of the numerical upwinding and GM/Redi contribution are most easily explored, and they are illustrated by a few simulations of the constant parameter QG Leith scheme at $L_d = 2.5\Delta s$ shown in Figure 8. In addition to the QG Leith run already described with upwinding and GM/Redi, one including upwinding and no GM/Redi, and two runs without upwinding were performed (replacing upwinding tracer advection with a minimally dissipative fourth-order centered scheme). In half of these runs, the GM/Redi transport coefficient κ_{GM} was set to zero, and in the other half $\kappa_{GM} = v_*$ as advocated here. A few conclusions may be drawn from Figure 8. (1) Energy spectral slope is less sensitive than potential enstrophy slope to tracer equation numerical discretization, and overall potential enstrophy at all scales is affected by the grid-scale dissipation and numerics. (2) The differences due to discretization are similar in magnitude to including or neglecting GM/Redi—neither effect is negligible, but both are much smaller than the differences among choices of viscosity scaling (Figure 6). (3) The fourth-order scheme including GM/Redi does not suffer the over-dissipation of potential enstrophy near the gridscale which occurs with all of the simulations using upwinding (Figure 7), but agreement in energy spectral slope is shared regardless of inclusion or neglect of GM/Redi and numerical scheme. Only in potential enstrophy slope is the combination of low dissipation numerics and inclusion of the GM/Redi contribution apparently preferable. Thus, the QG Leith tracer dissipation or numerical schemes are strong enough to contaminate large scales as measured by

Both forms of the Smagorinsky closure overdamp energy at small scales—somewhat more so in the harmonic as opposed to the biharmonic form (consistent with Griffies and Hallberg [2000]), as these simulations have slopes that are too steep near the gridscale. Interestingly, these schemes are among the best in the coarsest resolution simulations, where the Smagorinsky theory may be more appropriate as the grid-scale approaches the regime dominated by the inverse energy cascade, albeit with a spectral slope governed by vortex stretching instead of a kinetic energy cascade.

potential enstrophy statistics, but not as measured by kinetic energy spectral slope. Figure 6 recommends any QG Leith scheme to provide a robust scaling for kinetic energy, and Figures 7 and 8 recommend the use of the isoneutral GM/Redi diffusion—but performance will be limited if the numerical scheme is diffusive.

Hallberg [2013] and others argue that the inclusion of GM/Redi restratification in eddy-permitting simulations tends to compete for potential energy with the resolved eddies in such a way that the total (resolved plus parameterized) restratification cannot be maintained. How is it, then, that GM/Redi can be included in the QG Leith subgrid model without damping the resolved eddies? First, this effect may explain the decreased energy at the coarsest resolution (red lines) in the upper row of Figure 6. Second, the amount of additional restratification implied by GM under the QG Leith prescription of $\kappa_{GM} = v_*$ is significantly less at coarse resolution than is required to restore the total potential energy extraction—at least until the resolution is high enough to partially resolve the potential enstrophy cascade which is when the subgrid restratification fraction is small. The QG Leith subgrid model's GM restratification never rivals the resolved eddy restratification in magnitude, it is only sufficient to affect the potential energy and enstrophy dissipation at small scales (Figure 8).

To further explore this point, additional simulations were run with the GM/Redi coefficient set equal to the Smagorinsky and 2-D Leith viscosities. Consistent with our findings using QG Leith, there was nearly no difference in the spectra for 2-D Leith with GM/Redi on or off. In contrast, the larger Smagorinsky viscosity did manifest differences when used with GM/Redi (not shown); however, as Smagorinsky is inappropriate for the forward enstrophy cascade of MOLES, and has been shown to be overly dissipative in MOLES applications [e.g., Griffies and Hallberg, 2000], it is doubtful as a candidate for setting κ_{GM} and will not be considered further here.

The QG Leith prescribed eddy-induced diffusivity and viscosity result in very modest Pe_* and Re_* numbers. Because of the choice of $\kappa_{GM} = v_*$, the value of these dimensionless parameters is equal. Re_* is a measure of whether the gridscale is sufficiently viscous and can also indicate the susceptibility of the model to computational instability [e.g., Bryan *et al.*, 1975]. Likewise, a small or large Pe_* categorizes the stability of the tracer equation, and also influences the effect of numerical schemes (Figure 8). A small Re_* and Pe_* minimize spurious diapycnal mixing by keeping the flow smooth [Ilicak *et al.*, 2012]. Limiting spurious mixing maintains water mass properties and the overall global mean density structure [Griffies *et al.*, 2000]. For this reason, the horizontal mixing associated with upwinding is less desirable than the GM/Redi mixing from the QG Leith scheme (Figure 8), however the latter is computationally more expensive. Figure 9 compares the time-evolution of the domain-averaged $Re_* = Pe_*$ for each simulation using 2-D and QG Leith viscosities. Here the characteristic velocity scale V_* is taken as the mean absolute value of the cross-front velocity, since in the zonal mean the along-front velocity is not strained and does not feature gradients that contribute to dissipation. After about 200 days of spin-up, or 50 eddy turnover times, Re_* arrives and stays near one for both the $\Lambda = 1$ and $\epsilon = 8$ QG Leith simulations, whereas it remains $\gg 1$ for both the 2-D Leith and $\epsilon = 2$ QG Leith simulations.

The coarsest two simulation sets were designed to evaluate the performance of the QG Leith scheme in the limit when the resolution is not fine enough to resolve the inertial range of the forward enstrophy cascade. As noted by Hallberg [2013], even when eddies are resolved in some regions well, variations in stratification and Coriolis parameter mean that they may not be everywhere. Thus, if the QG Leith scheme is to be used in current-generation GCMs, it must fail gracefully when the potential enstrophy cascade is not resolved. On the positive side, the scheme remains numerically stable despite being used in a dynamical regime for which it was not designed, as is also true of the 2-D Leith scheme. The spectral slopes are roughly consistent with those predicted in the inverse energy cascade regime of large-scale QG turbulence or 2-D turbulence [Smith *et al.*, 2002]. However, the constant viscosity cases are able to better capture the average energy and enstrophy at large scales at the two coarsest resolutions. Nonetheless, 2-D Leith has been shown to be stable in this regime [e.g., Boer and Shepherd, 1983; Boccaletti *et al.*, 2007; Fox-Kemper and Menemenlis, 2008] and in the absence of a more appropriate dissipation method represents a suitable “endpoint” for QG Leith at the large scale.

The inclusion of GM/Redi coefficients as part of the QG Leith scheme is motivated by theoretical arguments. However, these terms also regularize the tracer equations and make the model resistant to shock formation,

just as upwinding does, but with more physical spectral behavior (Figure 8). Even without upwinding, the QG Leith scheme is viable and provides explicit lateral diffusivity (although monotonicity is not guaranteed). This lateral tracer transport inherits adiabatic physics from the use of the GM/Redi scheme, unlike upwinding in a z or σ coordinate model which causes spurious diapycnal diffusivity [Griffies *et al.*, 2000; Ilicak *et al.*, 2012].

4. Summary and Conclusion

In this paper a new subgrid scheme based on a quasi-geostrophic interpretation of the Leith [1996] scheme, named “QG Leith,” has been introduced. It is designed for use in models where quasi-geostrophic or 2-D dynamics dominate at the gridscale. The development of this scheme is motivated by a need for next-generation, scale-aware and flow-aware diffusivity and viscosity parameterizations in climate-scale GCMs.

The QG Leith scheme is motivated by analogous subgrid viscosity models for 3-D turbulence [Smagorinsky, 1963, 1993] and 2-D turbulence [Leith, 1968, 1996] common in LES modeling. Inspired by these models, the new scheme assumes that if the gridscale lies in the inertial range of the QG forward potential enstrophy cascade the viscous coefficient can be determined dynamically using the potential vorticity gradient of the resolved flow. The coefficient can be further tuned using an LES-style “test filter,” where the resolved enstrophy flux (assumed constant) is used to adjust v_* locally and in time. To facilitate this approach in a RANS model with complex bathymetry, a finite-difference-based spatial test filter [Sagaut and Grohens, 1999] is used instead of the usual spectral sharp-cutoff filter. Considerable computational expense and sensitivity to the choice of filter limits this approach in practice.

The QG Leith scheme has been shown to satisfy the requirements for a numerically stable, physically motivated subgrid model that is appropriate for the downscale enstrophy cascade regime of quasi-geostrophic turbulence. This regime is expected to be predominant in MOLES applications, and is distinct from the forward energy cascade regime where similar models like Smagorinsky are more appropriate. Though LES-style subgrid models may remain numerically stable when mismatched to the resolved dynamics, they may poorly reproduce the desired spectral characteristics (Figures 6 and 7) and amount of dissipation [e.g., Griffies and Hallberg, 2000].

Idealized simulations show that the energy and enstrophy spectra with QG Leith are greatly improved near the gridscale over other schemes and match the spectral slopes predicted from quasi-geostrophic turbulence theory. The grid Reynolds number for QG Leith is shown to asymptote to one, which is an important requirement to avoid spurious mixing [Ilicak *et al.*, 2012]. A limiter on the vortex stretching term is designed to ensure that the scheme remains numerically stable even when the forward enstrophy cascade is not resolved or when QG dynamics are not appropriate. Coarse-resolution experiments show that the spectral characteristics of QG Leith revert to 2-D Leith when the enstrophy dissipation scale is unresolved, as intended.

Further testing of the QG Leith scheme is necessary to evaluate its performance in less idealized settings, and is in progress. A particular focus of this ongoing work is the resultant kinetic energy balance from using the Leith schemes. The differences in the red lines in each panel of Figure 6 suggest that the choice of dissipation scheme affects the large-scale energy, but the idealized domain geometry and choice of boundary conditions in these models prevents a meaningful analysis here. Nonetheless, further testing in other idealized settings will also likely be fruitful. Lastly, the basic scheme introduced here has matched the viscosity with the tracer diffusivity at all depths. However, other relationships between these quantities [Smith and Marshall, 2009; Abernathey *et al.*, 2013] may prove more robust, improve the potential enstrophy spectra, and remove the need for ad hoc tapering schemes.

It is interesting to contemplate the highest resolution consistent with these schemes. Surely, the QG Leith scheme applies wherever QG dynamics dominate, and the extension to 2-D Leith extends the range of applicability into boundary layers and near the equator. The 2-D Leith scheme alone has been used in global models with approximately 2 km resolution [Rocha *et al.*, 2016], and at least in the ocean interior the asymptotics derived here predict that it, and QG Leith as well, remain appropriate even for large Fr_* , so long as $\epsilon Ro_*/M_{R_*}$ remains small in (16). Even when Ro_* becomes sufficiently large that ageostrophic currents begin to rival geostrophic ones, such as in mixed-layer eddies under submesoscale-permitting

resolution, the assumptions are only gently violated. When ageostrophic motions and overturning dominate at the small end of the submesoscale, i.e., where hydrostasy breaks down [Hamilton et al., 2014] or where the divergent wave spectrum begins to dominate the rotational vortex one [Capet et al., 2008; Callies et al., 2014], these Leith models are not appropriate and a scheme such as Smagorinsky [1993] or its anisotropic extensions [e.g., Ramachandran et al., 2013] is more theoretically grounded.

Finally, although the inspiring application here was oceanic, many coarse resolution climate models (e.g., T21 and T42) have *atmospheric model components* that are operating in the QG potential enstrophy cascade regime, which is observed to persist to roughly wave number 50 [Nastrom and Gage, 1985; Tulloch and Smith, 2006], so the QG Leith scheme may be appropriate in these models as well. As atmospheric modeling has proven, a big advantage of MOLES is that the largest eddies are resolved, rather than parameterized by the closure. Thus, phenomena that are hard to encapsulate in a parameterization—such as anisotropy [Maltrud and Vallis, 1991; Nazarenko and Quinn, 2009; Kamenkovich et al., 2009; Galperin et al., 2010; Fox-Kemper et al., 2013; Galperin et al., 2014], interactions with bottom topography [Maltrud and Holloway, 2008; Yeager, 2015], antidiiffusive behavior [Starr, 1968; Berloff, 2005], and potential vorticity constraints [Killworth, 1997]—are handled by the large, resolved eddies and can be ignored or handled simply in the subgrid model of small eddies.

Acknowledgments

S.B. gratefully acknowledges support from the Natural Environment Research Council (award NE/J010472/1). B.F.K. and B.P. were supported by NSF OCE 1350795. We would like to thank two anonymous reviewers, whose comments greatly improved this manuscript. Model data used in this research can be found at doi:10.7301/Z05X26VC.

References

- Abernathy, R., D. Ferreira, and A. Klocker (2013), Diagnostics of isopycnal mixing in a circumpolar channel, *Ocean Modell.*, 72, 1–16, doi: 10.1016/j.ocemod.2013.07.004.
- Adcock, S. T., and D. P. Marshall (2000), Interactions between geostrophic eddies and the mean circulation over large-scale bottom topography, *J. Phys. Oceanogr.*, 30(12), 3223–3238, doi:10.1175/1520-0485(2000)030<3223:IBGEAT>2.0.CO;2.
- Aiki, H., T. Jacobson, and T. Yamagata (2004), Parameterizing ocean eddy transports from surface to bottom, *J. Geophys. Res.*, 31, L19302, doi:10.1029/2004GL020703.
- Arbic, B. K., and G. R. Flierl (2004), Baroclinically unstable geostrophic turbulence in the limits of strong and weak bottom Ekman friction: Application to midocean eddies, *J. Phys. Oceanogr.*, 34(10), 2257–2273, doi:10.1175/1520-0485(2004)034<2257:BUGTIT>2.0.CO;2.
- Bachman, S. D., and B. Fox-Kemper (2013), Eddy parameterization challenge suite: I: Eady spindown, *Ocean Modell.*, 64, 12–28, doi:10.1016/j.ocemod.2012.12.003.
- Bachman, S. D., and J. R. Taylor (2014), Modelling of partially-resolved oceanic symmetric instability, *Ocean Modell.*, 82, 15–27, doi:10.1016/j.ocemod.2014.07.006.
- Bachman, S. D., B. Fox-Kemper, and F. O. Bryan (2015), A tracer-based inversion method for diagnosing eddy-induced diffusivity and advection, *Ocean Modell.*, 86, 1–14, doi:10.1016/j.ocemod.2014.11.006.
- Berloff, P. S. (2005), On dynamically consistent eddy fluxes, *Dyn. Atmos. Oceans*, 38(3), 123–146, doi:10.1016/j.dynatmoce.2004.11.003.
- Berloff, P., W. Dewar, S. Kravtsov, and J. McWilliams (2007), Ocean eddy dynamics in a coupled ocean-atmosphere model, *J. Phys. Oceanogr.*, 37, 1103–1121, doi:10.1175/JPO3041.1.
- Blaker, A. T., J. J. M. Hirschi, G. McCarthy, B. Sinha, S. Taws, R. Marsh, A. Coward, and B. de Cuevas (2015), Historical analogues of the recent extreme minima observed in the Atlantic meridional overturning circulation at 26°N, *Clim. Dyn.*, 44(1–2), 457–473, doi:10.1007/s00382-014-2274-6.
- Blumen, W. (1978), Uniform potential vorticity flow: Part I. Theory of wave interactions and two-dimensional turbulence, *J. Atmos. Sci.*, 35(5), 774–783, doi:10.1175/1520-0469(1978)035<0774:UPVFI>2.0.CO;2.
- Boccaletti, G., R. Ferrari, and B. Fox-Kemper (2007), Mixed layer instabilities and restratification, *J. Phys. Oceanogr.*, 37(9), 2228–2250, doi: 10.1175/JPO3101.1.
- Boer, G. J., and T. G. Shepherd (1983), Large-scale two-dimensional turbulence in the atmosphere, *J. Atmos. Sci.*, 40(1), 164–184, doi: 10.1175/1520-0469(1983)040<0164:LSTDII>2.0.CO;2.
- Brassington, G. B., et al. (2015), Progress and challenges in short-to medium-range coupled prediction, *J. Oper. Oceanogr.*, 8, suppl. 2, s239–s258, doi:10.1080/1755876X.2015.1049875.
- Bryan, F. O., R. Tomas, J. M. Dennis, D. B. Chelton, N. G. Loeb, and J. L. McClean (2010), Frontal scale air-sea interaction in high-resolution coupled climate models, *J. Clim.*, 23(23), 6277–6291, doi:10.1175/2010JCLI3665.1.
- Bryan, F. O., P. R. Gent, and R. Tomas (2014), Can Southern Ocean eddy effects be parameterized in climate models?, *J. Clim.*, 27(1), 411–425, doi:10.1175/JCLI-D-12-00759.1.
- Bryan, K., S. Manabe, and R. C. Pacanowski (1975), A global ocean-atmosphere climate model. Part II. The oceanic circulation, *J. Phys. Oceanogr.*, 5, 30–46, doi:10.1175/1520-0485(1975)005<0030:AGOACM>2.0.CO;2.
- Callies, J., R. Ferrari, and O. Bühler (2014), Transition from geostrophic turbulence to inertia-gravity waves in the atmospheric energy spectrum, *Proc. Natl. Acad. Sci. U. S. A.*, 111(48), 17,033–17,038, doi:10.1073/pnas.1410772111.
- Callies, J., G. Flierl, R. Ferrari, and B. Fox-Kemper (2016), The role of mixed-layer instabilities in submesoscale turbulence, *J. Fluid Mech.*, 788, 5–41, doi:10.1017/jfm.2015.700.
- Capet, X., J. C. McWilliams, M. J. Molemaker, and A. F. Shchepetkin (2008), Mesoscale to submesoscale transition in the California Current system. Part III: Energy balance and flux, *J. Phys. Oceanogr.*, 38(10), 2256–2269, doi:10.1175/2008JPO3810.1.
- Charney, J. G. (1971), Geostrophic turbulence, *J. Atmos. Sci.*, 28(6), 1087–1095, doi:10.1175/1520-0469(1971)028<1087:GT>2.0.CO;2.
- Chassignet, E. P., and Z. D. Garraffo (2001), Viscosity parameterization and the Gulf Stream separation. From stirring to mixing in a stratified ocean, paper presented at Proceedings of Aha Huliko'a Hawaiian Winter Workshop, Univ. of Hawaii at Manoa, Honolulu.
- Chelton, D. B., R. A. DeSzoeke, M. G. Schlax, K. El Naggar, and N. Siwertz (1998), Geographical variability of the first baroclinic Rossby radius of deformation, *J. Phys. Oceanogr.*, 28(3), 433–460, doi:10.1175/1520-0485(1998)028<0433:GRD>2.0.CO;2.
- Chemke, R., and Y. Kaspi (2015), The latitudinal dependence of atmospheric jet scales and macroturbulent energy cascades, *J. Atmos. Sci.*, 72(10), 3891–3907, doi:10.1175/JAS-D-15-0007.1.

- Chen, Q., M. Gunzburger, and T. Ringler (2011), A scale-invariant formulation of the anticipated potential vorticity method, *Mon. Weather Rev.*, 139(8), 2614–2629, doi:10.1175/MWR-D-10-05004.1.
- de Szoeke, R. A., and A. F. Bennett (1993), Microstructure fluxes across density surfaces, *J. Phys. Oceanogr.*, 23(10), 2254–2264, doi:10.1175/1520-0485(1993)023<2254:MFADS>2.0.CO;2.
- Delworth, T., et al. (2012), Simulated climate and climate change in the GFDL CM2.5 high-resolution coupled climate model, *J. Clim.*, 25, 2755–2781, doi:10.1175/JCLI-D-11-0316.1.
- Dukowicz, J., and R. Smith (1997), Stochastic theory of compressible turbulent fluid transport, *Phys. Fluids*, 9, 3523–3529, doi:10.1063/1.869460.
- Eady, E. T. (1949), Long waves and cyclone waves, *Tellus*, 1(3), 33–52, doi:10.1111/j.2153-3490.1949.tb01265.x.
- Farrell, B. F., and P. J. Ioannou (1993), Stochastic dynamics of baroclinic waves, *J. Atmos. Sci.*, 50(24), 4044–4057, doi:10.1175/1520-0469(1993)050<4044:SDOBW>2.0.CO;2.
- Ferrari, R., J. C. McWilliams, V. Canuto, and M. Dubovikov (2008), Parameterization of eddy fluxes near oceanic boundaries, *J. Clim.*, 21, 2770–2789, doi:10.1175/2007JCLI1510.1.
- Ferrari, R., S. M. Griffies, A. J. Nurser, and G. K. Vallis (2010), A boundary-value problem for the parameterized mesoscale eddy transport, *Ocean Modell.*, 32(3), 143–156, doi:10.1016/j.ocemod.2010.01.004.
- Fox-Kemper, B., and D. Menemenlis (2008), Can large eddy simulation techniques improve mesoscale rich ocean models?, in *Ocean Modeling in an Eddying Regime*, *Geophys. Monogr. Ser.*, vol. 177, edited by M. W. Hecht and H. Hasumi, pp. 319–337, AGU, Washington, D. C., doi:10.1029/177GM19.
- Fox-Kemper, B., R. Ferrari, and R. Hallberg (2008), Parameterization of mixed layer eddies. Part I: Theory and diagnosis, *J. Phys. Oceanogr.*, 38(6), 1145–1165, doi:10.1175/2007JPO3792.1.
- Fox-Kemper, B., G. Danabasoglu, R. Ferrari, S. M. Griffies, R. W. Hallberg, M. M. Holland, M. E. Maltrud, S. Peacock, and B. L. Samuels (2011), Parameterization of mixed layer eddies. III: Implementation and impact in global ocean climate simulations, *Ocean Modell.*, 39, 61–78, doi:10.1016/j.ocemod.2010.09.002.
- Fox-Kemper, B., R. Lumpkin, and F. O. Bryan (2013), Lateral transport in the ocean interior, in *Ocean Circulation and Climate: A 21st Century Perspective*, edited by G. Siedler et al., pp. 185–209, Elsevier, Cambridge, Mass., doi:10.1016/B978-0-12-391851-2.00008-8.
- Frenger, I., N. Gruber, R. Knutti, and M. Münnich (2013), Imprint of Southern Ocean eddies on winds, clouds and rainfall, *Nat. Geosci.*, 6(8), 608–612, doi:10.1038/ngeo1863.
- Galperin, B., S. Sukoriansky, and N. Dikovskaya (2010), Geophysical flows with anisotropic turbulence and dispersive waves: Flows with a β -effect, *Ocean Dyn.*, 60(2), 427–441, doi:10.1007/s10236-010-0278-2.
- Galperin, B., R. M. Young, S. Sukoriansky, N. Dikovskaya, P. L. Read, A. J. Lancaster, and D. Armstrong (2014), Cassini observations reveal a regime of zonostrophic macroturbulence on Jupiter, *Icarus*, 229, 295–320, doi:10.1016/j.icarus.2013.08.030.
- Gent, P. R., and J. C. McWilliams (1990), Isopycnal mixing in ocean circulation models, *J. Phys. Oceanogr.*, 20, 150–155, doi:10.1175/1520-0485(1990)020<0150:IMOCM>2.0.CO;2.
- Germano, M. (1992), Turbulence: The filtering approach, *J. Fluid Mech.*, 238, 325–336, doi:10.1017/S0022112092001733.
- Germano, M., U. Piomelli, P. Moin, and W. H. Cabot (1991), A dynamic subgrid-scale eddy viscosity model, *Phys. Fluids*, 3(7), 1760–1765, doi:10.1063/1.857955.
- Geurts, B. J., and D. D. Holm (2006), Leray and LANS- α modelling of turbulent mixing, *J. Turbulence*, 7, N10, doi:10.1080/1468524050051601.
- Ghosal, S., T. S. Lund, P. Moin, and K. Akselvoll (1995), A dynamic localization model for large-eddy simulation of turbulent flows, *J. Fluid Mech.*, 286, 229–255, doi:10.1017/S0022112095000711.
- Griffies, S. M. (1998), The Gent-McWilliams skew flux, *J. Phys. Oceanogr.*, 28(5), 831–841, doi:10.1175/1520-0485(1998)028<0831:TGMSF>2.0.CO;2.
- Griffies, S. M., and R. W. Hallberg (2000), Biharmonic friction with a Smagorinsky-like viscosity for use in large-scale eddy-permitting ocean models, *Mon. Weather Rev.*, 128(8), 2935–2946, doi:10.1175/1520-0493(2000)128<2935:BFWASL>2.0.CO;2.
- Griffies, S. M., R. C. Pacanowski, and R. W. Hallberg (2000), Spurious diapycnal mixing associated with advection in a z-coordinate ocean model, *Mon. Weather Rev.*, 128, 538–564, doi:10.1175/1520-0493(2000)128<0538:SDMAWA>2.0.CO;2.
- Hallberg, R. (2013), Using a resolution function to regulate parameterizations of oceanic mesoscale eddy effects, *Ocean Modell.*, 72, 92–103, doi:10.1016/j.ocemod.2013.08.007.
- Hamiltonton, P. E., L. P. Van Roeke, B. Fox-Kemper, K. Julien, and G. P. Chini (2014), Langmuir-submesoscale interactions: Descriptive analysis of multiscale frontal spin-down simulations, *J. Phys. Oceanogr.*, 44(9), 2249–2272, doi:10.1175/JPO-D-13-0139.1.
- Hecht, M. W., M. R. Petersen, B. A. Wingate, E. Hunke, and M. Maltrud (2008), Lateral mixing in the eddying regime and a new broad-ranging formulation, in *Ocean Modeling in an Eddying Regime*, vol. 177, edited by M. W. Hecht and H. Hasumi, pp. 339–352, AGU, Washington, D. C., doi:10.1029/177GM20.
- Held, I. M., R. T. Pierrehumbert, S. T. Garner, and K. L. Swanson (1995), Surface quasi-geostrophic dynamics, *J. Fluid Mech.*, 282, 1–20, doi:10.1017/S0022112095000012.
- Ilicak, M., T. M. Özgökmen, H. Peters, Z. H. Baumert, and M. Iskandarani (2008), Very large eddy simulation of the Red Sea overflow, *Ocean Modell.*, 20, 183–206, doi:10.1016/j.ocemod.2007.08.002.
- Ilicak, M., A. J. Adcroft, S. M. Griffies, and R. W. Hallberg (2012), Spurious dianeutral mixing and the role of momentum closure, *Ocean Modell.*, 45, 37–58, doi:10.1016/j.ocemod.2011.10.003.
- Jansen, M. F., and I. M. Held (2014), Parameterizing subgrid-scale eddy effects using energetically consistent backscatter, *Ocean Modell.*, 80, 36–48, doi:10.1016/j.ocemod.2014.06.002.
- Jochum, M., G. Danabasoglu, M. Holland, Y. O. Kwon, and W. G. Large (2008), Ocean viscosity and climate, *J. Geophys. Res.*, 113, C06017, doi:10.1029/2007JC004515.
- Jochum, M., B. P. Briegleb, G. Danabasoglu, W. G. Large, N. J. Norton, S. R. Jayne, M. H. Alford, and F. O. Bryan (2013), The impact of oceanic near-inertial waves on climate, *J. Clim.*, 26(9), 2833–2844, doi:10.1175/JCLI-D-12-00181.1.
- Kamenkovich, I., P. Berloff, and J. Pedlosky (2009), Anisotropic material transport by eddies and eddy-driven currents in a model of the North Atlantic, *J. Phys. Oceanogr.*, 39(12), 3162–3175, doi:10.1175/2009JPO4239.1.
- Killworth, P. D. (1997), On the parameterization of eddy transfer Part I. Theory, *J. Mar. Res.*, 55(6), 1171–1197, doi:10.1357/0022240973224102.
- Kirtman, B. P., et al. (2012), Impact of ocean model resolution on CCSM climate simulations, *Clim. Dyn.*, 39(6), 1303–1328, doi:10.1007/s00382-012-1500-3.
- Kolmogorov, A. N. (1941), The local structure of turbulence in incompressible viscous fluid for very large Reynolds numbers, *Dokl. Akad. Nauk SSSR*, 30(4), 9–13, doi:10.1098/rspa.1991.0075.
- Kraichnan, R. H., 1967. Inertial ranges in two-dimensional turbulence, *Phys. Fluids*, 16, 1417–1423, doi:10.1063/1.1762301.

- Lapeyre, G., and P. Klein (2006), Dynamics of the upper oceanic layers in terms of surface quasigeostrophy theory, *J. Phys. Oceanogr.*, 36(2), 165–176, doi:10.1175/JPO2840.1.
- Large, W. G., G. Danabasoglu, S. C. Doney, and J. C. McWilliams (1997), Sensitivity to surface forcing and boundary layer mixing in a global ocean model: Annual-mean climatology, *J. Phys. Oceanogr.*, 27(11), 2418–2447, doi:10.1175/1520-0485(1997)027<2418:STSFAB>2.0.CO;2.
- Larichev, V. D., and J. C. McWilliams (1991), Weakly decaying turbulence in an equivalent-barotropic fluid, *Phys. Fluids*, 3(5), 938–950, doi:10.1063/1.857970.
- LeBlond, P. H., and L. A. Mysak (1981), *Waves in the Ocean*, vol. 20, Elsevier, New York.
- Leith, C. E. (1968), Diffusion approximation for two-dimensional turbulence, *Phys. Fluids*, 10, 1409–1416, doi:10.1063/1.1691968.
- Leith, C. E. (1996), Stochastic models of chaotic systems, *Physica D*, 98, 481–491, doi:10.1016/0167-2789(96)00107-8.
- Leonard, A. (1974), Energy cascade in large-eddy simulations of turbulent fluid flows, *Adv. Geophys.*, 18, 237–248, doi:10.1016/S0065-2687(08)60464-1.
- Lesieur, M., O. Métais, and P. Comte (2005), *Large-Eddy Simulations of Turbulence*, Cambridge Univ. Press, Cambridge, U. K.
- Le Traon, P. Y., P. Klein, B. L. Hua, and G. Dibarboore (2008), Do altimeter wavenumber spectra agree with the interior or surface quasigeostrophic theory?, *J. Phys. Oceanogr.*, 38(5), 1137–1142, doi:10.1175/2007JPO3806.1.
- Lilly, D. K. (1992), A proposed modification of the Germano subgrid-scale closure method, *Phys. Fluids*, 4(3), 633–635, doi:10.1063/1.858280.
- Liu, S., C. Meneveau, and J. Katz (1995), Experimental study of similarity subgrid-scale models of turbulence in the far-field of a jet, *Appl. Sci. Res.*, 54(3), 177–190, doi:10.1007/BF00849115.
- Lund, T. S. (1997), On the use of discrete filters for large eddy simulation. *Annual Research Briefs*, 83–95.
- Maltrud, M. E., and G. Holloway (2008), Implementing biharmonic neptune in a global eddying ocean model, *Ocean Model.*, 21(1), 22–34, doi:10.1016/j.ocemod.2007.11.003.
- Maltrud, M. E., and G. K. Vallis (1991), Energy spectra and coherent structures in forced two-dimensional and beta-plane turbulence, *J. Fluid Mech.*, 228, 321–342, doi:10.1017/S0022112091002720.
- Marshall, J., and G. Shutts (1981), A note on rotational and divergent eddy fluxes, *J. Phys. Oceanogr.*, 11(12), 1677–1680, doi:10.1175/1520-0485(1981)011<1677:ANORAD>2.0.CO;2.
- Marshall, J., A. Adcroft, C. Hill, L. Perelman, and C. Heisey (1997), A finite-volume, incompressible Navier Stokes model for studies of the ocean on parallel computers, *J. Geophys. Res.*, 102, 5753–5766, doi:10.1029/96JC02775.
- McClean, J. L., et al. (2011), A prototype two-decade fully-coupled fine-resolution CCSM simulation, *Ocean Model.*, 39(1), 10–30, doi:10.1016/j.ocemod.2011.02.011.
- McWilliams, J. C. (1985), A uniformly valid model spanning the regimes of geostrophic and isotropic, stratified turbulence: Balanced turbulence, *J. Atmos. Sci.*, 42(16), 1773–1774, doi:10.1175/1520-0469(1985)042<1773:AUVMST>2.0.CO;2.
- McWilliams, J. C., and P. Sullivan (2000), Vertical mixing by Langmuir circulations, *Spill Sci. Technol. Bull.*, 6(3–4), 225–237, doi:10.1016/S1353-2561(01)00041-X.
- McWilliams, J. C., P. Sullivan, and C. Moeng (1997), Langmuir turbulence in the ocean, *J. Fluid Mech.*, 334, 1–30, doi:10.1017/S0022112096004375.
- Meneveau, C., and J. Katz (2000), Scale-invariance and turbulence models for large-eddy simulation, *Ann. Rev. Fluid Mech.*, 32(1), 1–32, doi:10.1146/annurev.fluid.32.1.1.
- Meneveau, C., T. S. Lund, and W. H. Cabot (1996), A Lagrangian dynamic subgrid-scale model of turbulence, *J. Fluid Mech.*, 319, 353–385, doi:10.1017/S0022112096007379.
- Mizielinski, M. S., et al. (2014), High-resolution global climate modelling: The UPSCALE project, a large-simulation campaign, *Geosci. Model Dev.*, 7(4), 1629–1640, doi:10.5194/gmd-7-1629-2014.
- Mohseni, K., B. Kosović, S. Shkoller, and J. E. Marsden (2003), Numerical simulations of the Lagrangian averaged Navier-Stokes equations for homogeneous isotropic turbulence, *Phys. Fluids*, 15(2), 524–544, doi:10.1063/1.1533069.
- Munk, W. H. (1950), On the wind-driven ocean circulation, *J. Meteorol.*, 7(2), 80–93, doi:10.1175/1520-0469(1950)007<0080:OTW-DOC>2.0.CO;2.
- Nadiga, B. T., and F. Bouchet (2011), The equivalence of the Lagrangian-averaged Navier-Stokes- α model and the rational large eddy simulation model in two dimensions, *Phys. Fluids*, 23(9), 095105, doi:10.1063/1.3632084.
- Najjar, F. M., and D. K. Tafti (1996), Study of discrete test filters and finite difference approximations for the dynamic subgrid-scale stress model, *Phys. Fluids*, 8(4), 1076–1088, doi:10.1063/1.868887.
- Nastrom, G. D., and K. S. Gage (1985), A climatology of atmospheric wavenumber spectra of wind and temperature observed by commercial aircraft, *J. Atmos. Sci.*, 42(9), 950–960, doi:10.1175/1520-0469(1985)042<0950:ACOAWS>2.0.CO;2.
- Nazarenko, S., and B. Quinn (2009), Triple cascade behavior in quasigeostrophic and drift turbulence and generation of zonal jets, *Phys. Rev. Lett.*, 103(11), 118501, doi:10.1103/PhysRevLett.103.118501.
- Nguyen, A. T., D. Menemenlis, and R. Kwok (2011), Arctic ice-ocean simulation with optimized model parameters: Approach and assessment, *J. Geophys. Res.*, 116, C04025, doi:10.1029/2010JC006573.
- Pedlosky, J. (1987), *Geophysical Fluid Dynamics*, Springer-Verlag, New York.
- Penduff, T., M. Juza, L. Brodeau, G. Smith, B. Barnier, J.-M. Molines, A.-M. Treguier, and G. Madec (2010), Impact of global ocean model resolution on sea-level variability with emphasis on interannual time scales, *Ocean Sci.*, 6(1), 269–284, doi:10.5194/os-6-269-2010.
- Pierrehumbert, R. T., I. M. Held, and K. L. Swanson (1994), Spectra of local and nonlocal two-dimensional turbulence, *Chaos Solitons Fractals*, 4(6), 1111–1116, doi:10.1016/0960-0779(94)90140-6.
- Pietarila Graham, J., and T. Ringler (2013), A framework for the evaluation of turbulence closures used in mesoscale ocean large-eddy simulations, *Ocean Model.*, 65, 25–39, doi:10.1016/j.ocemod.2013.01.004.
- Piomelli, U. (1993), High Reynolds number calculations using the dynamic subgrid-scale stress model, *Phys. Fluids A*, 5(6), 1484–1490, doi:10.1063/1.858586.
- Piomelli, U., and J. Liu (1995), Large-eddy simulation of rotating channel flows using a localized dynamic model, *Phys. Fluids*, 7(4), 839–848, doi:10.1063/1.868607.
- Piomelli, U., and T. A. Zang (1991), Large-eddy simulation of transitional channel flow, *Comput. Phys. Commun.*, 65(1–3), 224–230, doi:10.1016/0010-4655(91)90175-K.
- Ramachandran, S., A. Tandon, and A. Mahadevan (2013), Effect of subgrid-scale mixing on the evolution of forced submesoscale instabilities, *Ocean Model.*, 66, 45–63, doi:10.1016/j.ocemod.2013.03.001.
- Redi, M. H. (1982), Oceanic isopycnal mixing by coordinate rotation, *J. Phys. Oceanogr.*, 12, 1154–1158, doi:10.1175/1520-0485(1982)012<1154:OIMCR>2.0.CO;2.
- Rhines, P. B., and Young, W. R. (1982), Homogenization of potential vorticity in planetary gyres, *J. Fluid Mech.*, 122, 347–367, doi:10.1017/S0022112082002250.

- Ringler, T., M. Petersen, R. L. Higdon, D. Jacobsen, P. W. Jones, and M. Maltrud (2013), A multi-resolution approach to global ocean modeling, *Ocean Model.*, 69, 211–232, doi:10.1016/j.ocemod.2013.04.010.
- Roberts, M. J., and D. P. Marshall (1998), Do we require adiabatic dissipation schemes in eddy-resolving models?, *J. Phys. Oceanogr.*, 28, 2050–2063, doi:10.1175/1520-0485(1998)028<2050:DWRADS>2.0.CO;2.
- Rocha, C. B., T. K. Chereskin, S. T. Gille, and D. Menemenlis (2016), Mesoscale to submesoscale wavenumber spectra in Drake Passage, *J. Phys. Oceanogr.*, 46(2), 601–620, doi:10.1175/JPO-D-15-0087.1.
- Rubio, A. M., K. Julien, E. Knobloch, and J. B. Weiss (2014), Upscale energy transfer in three-dimensional rapidly rotating turbulent convection, *Phys. Rev. Lett.*, 112(14), 144501, doi:10.1103/PhysRevLett.112.144501.
- Sagaut, P. (2005), *Large Eddy Simulation for Incompressible Flows*, Springer, Heidelberg, Germany.
- Sagaut, P., and R. Grohens (1999), Discrete filters for large eddy simulation, *Int. J. Numer. Methods Fluids*, 31(8), 1195–1220, doi:10.1002/(SICI)1097-0363(19991230)31:8<1195::AID-FLD914>3.0.CO;2-H.
- Salmon, R. (1978), Two-layer quasi-geostrophic turbulence in a simple special case, *Geophys. Astrophys. Fluid Dyn.*, 10(1), 25–52, doi:10.1080/03091927808242628.
- San, O., A. E. Staples, and T. Iliescu (2013), Approximate deconvolution large eddy simulation of a stratified two-layer quasigeostrophic ocean model, *Ocean Model.*, 63, 1–20, doi:10.1016/j.ocemod.2011.08.003.
- Scott, R. B., and F. Wang (2005), Direct evidence of an oceanic inverse kinetic energy cascade from satellite altimetry, *J. Phys. Oceanogr.*, 35(9), 1650–1666, doi:10.1175/JPO2771.1.
- Scott, R. B., B. K. Arbic, E. P. Chassignet, A. C. Coward, M. Maltrud, W. J. Merryfield, A. Srinivasan, and A. Varghese (2010), Total kinetic energy in four global eddying ocean circulation models and over 5000 current meter records, *Ocean Model.*, 32(3–4), 157–169, doi:10.1016/j.ocemod.2010.01.005.
- Smagorinsky, J. (1963), General circulation experiments with the primitive equations: I. The basic experiment, *Mon. Weather Rev.*, 91(3), 99–164, doi:10.1175/1520-0493(1963)091<0099:GCEWTP>2.3.CO;2.
- Smagorinsky, J. (1993), Some historical remarks on the use of nonlinear viscosities, in *Large Eddy Simulation of Complex Engineering and Geophysical Flows*, edited by B. Galperin and S. A. Orszag, Cambridge Univ. Press, Cambridge, U. K.
- Smith, K. S., and J. Marshall (2009), Evidence for enhanced eddy mixing at mid-depth in the Southern Ocean, *J. Phys. Oceanogr.*, 39, 50–69, doi:10.1175/2008JPO3880.1.
- Smith, K. S., G. Boccaletti, C. C. Henning, I. Marinov, C. Y. Tam, I. M. Held, and G. K. Vallis (2002), Turbulent diffusion in the geostrophic inverse cascade, *J. Fluid Mech.*, 469, 13–48, doi:10.1017/S0022112002001763.
- Starr, V. P. (1968), *Physics of Negative Viscosity Phenomena*, McGraw-Hill, New York.
- Thompson, A. F., and W. R. Young (2007), Two-layer baroclinic eddy heat fluxes: Zonal flows and energy balance, *J. Atmos. Sci.*, 64(9), 3214–3231, doi:10.1175/JAS4000.1.
- Treguier, A., J. Deshayes, J. Le Sommer, C. Lique, G. Madec, T. Penduff, J.-M. Molines, B. Barnier, R. Bourdalle-Badie, and C. Talandier (2014), Meridional transport of salt in the global ocean from an eddy-resolving model, *Ocean Sci.*, 10(2), 243–255, doi:10.5194/os-10-243-2014.
- Tulloch, R., and K. S. Smith (2006), A theory for the atmospheric energy spectrum: Depth-limited temperature anomalies at the tropopause, *Proc. Natl. Acad. Sci. U. S. A.*, 103(40), 14,690–14,694, doi:10.1073/pnas.0605494103.
- Vallis, G. K. (2006), *Atmospheric and Oceanic Fluid Dynamics: Fundamentals and Large-Scale Circulation*, Cambridge Univ. Press, Cambridge, U. K.
- Vreman, B. (1995), Direct and large-eddy simulation of the temporal, turbulent compressible mixing layer, PhD thesis, Univ. of Twente, Enschede, Netherlands.
- Willebrand, J., B. Barnier, C. Boning, C. Dieterich, P. Killworth, C. Le Provost, Y. Jia, J. Molines, and A. New (2001), Circulation characteristics in three eddy-permitting models of the North Atlantic, *Prog. Oceanogr.*, 48, 123–161, doi:10.1016/S0079-6611(01)00003-9.
- Wilson, C., and R. G. Williams (2004), Why are eddy fluxes of potential vorticity difficult to parameterize?, *J. Phys. Oceanogr.*, 34(1), 142–155, doi:10.1175/1520-0485(2004)034<0142:WAEFOP>2.0.CO;2.
- Wright, D. G., R. Pawlowicz, T. J. McDougall, R. Feistel, and G. M. Marion (2011), Absolute salinity, “density salinity” and the reference-composition salinity scale: Present and future use in the seawater standard TEOS-10, *Ocean Sci.*, 7(1), 1–26, doi:10.5194/os-7-1-2011.
- Yeager, S. (2015), Topographic coupling of the Atlantic overturning and gyre circulations, *J. Phys. Oceanogr.*, 45(5), 1258–1284, doi:10.1175/JPO-D-14-0100.1.
- Young, W. R. (2012), An exact thickness-weighted average formulation of the Boussinesq equations, *J. Phys. Oceanogr.*, 42(5), 692–707, doi:10.1175/JPO-D-11-0102.1.